Asymmetries in Semi-Inclusive Deep-Inelastic $(e, e'\pi^{\pm})$ Reactions on a Longitudinally Polarized ^{3}He Target at 8.8 and 11 GeV

J. Arrington, R. Dupre, A. El Alaoui, K. Hafidi, R. J. Holt, P. E. Reimer, and X. Zhan

Argonne National Laboratory

A. Kolarkar

Boston University, Boston, MA

X. Qian

California Institute of Technology, Pasadena, CA

K. Aniol and D. J. Margaziotis

California State University-Los Angles, Los Angles, CA

X.Z. Bai, H.X. He, S.Y. Hu, X.M. Li, H.H. Xia, L. Ye, J. Yuan, J. Zhou, and S.H. Zhou

China Institute of Atomic Energy, Beijing, P. R. China

D. Armstrong, T. Averett, P. Bradshaw, and B. Zhao

College of William & Mary, Williamburg, VA

H. Gao, M. Huang, G. Laskaris, S. Malace, C. Peng, Q.J. Ye, and Y. Zhang

Duke University and the Triangle Universities Nuclear Laboratory, Durham, NC

P. Markowitz and L. Guo

Florida International University, Miami, FL

R. Subedi

George Washington University, Washington, D.C

Y. Li and L.Y. Zhu

Hampton University, Hampton, VA

H.P. Cheng, R.C. Liu, H.J. Lu, and Y. Shi

Huangshan University, Huangshan, P. R. China

X.S. Chen and N. Li

Huazhong University of Science and Technology, Wuhan, China

U. D'Alesio and F. Murgia

Cagliari University and INFN, Cagliari, Italy

R. De Leo, L. Lagamba, S. Marrone, G. Simonetti, and I. Vilardi

INFN-Bari and University of Bari, Bari, Italy

E. De Sanctis, M. Mirazita, S. A. Pereira, and P. Rossi

INFN Laboratori Nazionali di Frascati, Frascati, Italy

A. Bacchetta and B. Pasquini

Università di Pavia and INFN, Pavia, Italy

V. Bellini, F. Mammoliti, F. Noto, G. Russo, and C.M. Sutera

University of Catania and INFN/Catania, Catania , Italy

S. Scopetta

University degi Studi di Perguria, INFN, Perugia, Italy

E. Pace

Rome-Tor Vergata University, Rome, Italy

E. Cisbani, F. Cusanno, S. Frullani, F. Garibaldi, G. Salme', and G. M. Urciuoli

INFN-Roma and gruppo collegato Sanitá, Rome, Italy

M. Anselmino and M. Boglione

Torino University and INFN, Torino, Italy

A. Afanasev, H. Avagyan, K. Allada, A. Camsonne, J.-P. Chen (Co-spokesperson),
E. Chudakov, A. Deur, J. Gomez, D. W. Higinbotham, J. O. Hansen,
C. W. de Jager, M. Jones, J. LeRose, R. Michaels, B. Musch,
S. Nanda, A. Prokudin, Y. Qiang (Co-spokesperson), A. Saha,
M. Schlegel, B. Sawatzky, B. Wojtsekhowski, and J. Zhang

Thomas Jefferson National Accelerator Facility, Newport News, VA, 23606

M. Mihovilovič and S. Širca

Jožef Stefan Institute, Liubljana, Slovenia

B.T. Hu and Y. Zhang

Lanzhou University, Lanzhou, P. R. China

F. Yuan

Lawrence Berkeley National Laboratory, Berkeley, CA

T. Holmstrom

Longwood University, Farmville, VA

X. Jiang, M.X. Liu, and A. Puckett

Los Alamos National Laboratory, Los Alamos, NM

W. Bertozzi, S. Gilad, J. Huang (Co-spokesperson/Contact),*

A. Kelleher, N. Muangma, K. Pan, and V. Sulkosky

Massachusetts Institute of Technology, Cambridge, MA

J. Dunne and D. Dutta

Mississippi State University, Starkville, MS

M. Burkardt

New Mexico State University, Las Cruces, NM

L. Weinstein

Old Dominion University, Norfolk, VA

B.-Q. Ma and Y.J. Mao

School of Physics, Peking University, P. R. China

L. Gamberg

Pennsylvania State University at Berks, Reading, PA

B. Xiao

Pennsylvania State University, University Park, PA

L. El Fassi, R. Gilman, G. Kumbartzki, R. Ransome, E. Schulte, and Y.W. Zhang

Rutgers University, Piscataway, NJ

Seonho Choi, Hoyoung Kang, Hyekoo Kang, Byungwuek Lee, and Yoomin Oh

Seoul National University, Seoul, Korea

Z.T. Liang and X.T. Huang

Shandong University, Jinan, China

A. J. Sarty

St. Mary's University, Halifax, Nova Scotia, Canada

P. Souder and R. Holmes

Syracuse University, Syracuse, NY

E. Piasetzky and I. Pomerantz

Tel aviv University, Tel Aviv, Israel

W. Armstrong, Z.-E. Meziani, N. Sparveris, and H. Yao

Temple University, Philadelphia, PA

W.-C. Ding, Y.L. Li, J.-B. Wang, Y. Wang, and Z.G. Xiao

Tsinghua University, Beijing, P. R. China

P. Schweitzer

University of Connecticut, Storrs, CT

J. Annand, D. Hamilton, D. Ireland, R. Kaiser, K. Livingston,
I.J.D. MacGregor, D. Protopopescu, G. Rosner, and B. Seitz

University of Glasgow, Glasgow, Scotland

A. Nathan, N. Makins, J.-C. Peng, and Y. Wang

University of Illinois, Urbana-Champaign, IL

W. Korsch

University of Kentucky, Lexington, KY

E.J. Beise

University of Maryland, College Park, MD

K. Kumar

University of Massachusetts, Amherst, MA

C. Dutta

University of Michigan, Ann Arbor, MI

S. Phillips and K. Slifer

University of New Hampshire, Durham, NH

K. Hu, M. Shao, X. L. Wang, Z. Z. Xu, X. Yan, W. B. Yan (Co-spokesperson),
Y. Ye, Y. X. Zhao, Z. G. Zhao, Z. Y. Zhang, and P. J. Zhu

University of Science and Technology of China, Hefei, P. R. China

G. Cates, M. Dalton, R. Lindgren, N. Liyanage, V. Nelyubin, B. Norum,
K. Paschke, M. H. Shabestari, W. A. Tobias, K. Wang, Z. Zhao, and X.C. Zheng

University of Virginia, Charlottesville, VA

and the HallA Collaboration

Abstract

We propose a measurement of single-target and double spin azimuthal asymmetries (SSAs and DSAs) in semi-inclusive electroproduction of charged pions, using the upgraded CEBAF electron beam, the Hall A polarized ^{3}He target as an effective polarized neutron target, and the newly approved SoLID spectrometer. The hardware setup is similar to that of experiment E12-10-006, with additional requirements of a longitudinally polarized target and a polarized beam. We also request a high beam polarization for E12-10-006 to measure DSAs with a transversely polarized target. The SSAs and DSAs, with longitudinal and transverse target spin, respectively, are related to two "worm-gear" transverse-momentum-dependent (TMD) parton distributions of the nucleon at leading twist. Both of the "worm-gear" TMD distributions require an interference between wave function components that differ by one unit of quark orbital angular momentum (OAM), as explicitly shown in several models. In addition, the DSAs with a longitudinal target spin will constrain the flavor decomposition of the quark helicity distribution of the nucleon and provide information on their transverse momentum dependence. All asymmetries will be measured with a high precision and a large kinematic coverage in a 4-D phase space of x, z, $P_{h\perp}$ and Q^2. The systematic uncertainties are improved by fast target spin flips and a large coverage in the azimuthal angles. We request 35 PAC days of data taking on the longitudinally polarized ^{3}He target.

*Electronic address: jinhuang@jlab.org

Contents

1. INTRODUCTION

Deep inelastic scattering (DIS) has been used extensively as an important testing ground for QCD. Over the past four decades, many DIS experiments have been devoted to the detailed studies of parton momentum and helicity distributions inside nucleons. Together with the related hard-scattering processes initiated by nucleons, data from these experiments were used to extract collinear parton distribution functions (PDFs) in the quark-parton model [1], which include the parton density distribution, f_1^q, and the parton helicity distribution, g_1^q. Both of distributions are functions of the parton longitudinal momentum fraction, x and the photon virtuality, Q^2. The comparison of unpolarized DIS structure functions in the large Q^2 range with the QCD evolution equation has provided one of the best tests of QCD. Meanwhile, the spin structure of the nucleon has attracted great interest since the "spin-crisis" from the European Muon Collaboration (EMC) experiments in the 1980s [2], which suggested that the helicity of quarks accounts for only a small fraction of the nucleon spin. The sequential intensive experimental and theoretical investigations that followed the "spin-crisis" have resulted in a great deal of knowledge on the partonic origin of the nucleon longitudinal spin structure. We have also learned that the quark orbital motion and the transverse structure are essential parts of the partonic spin and momentum substructure of the nucleon.

A new phase of investigation has been started by studying physical observables that are sensitive to the transverse momentum structure of nucleons. This information is encoded in the Transverse Momentum Dependent (TMD) parton distributions, which link the intrinsic motion of partons to their spin and the spin of the parent nucleon. At leading twist, there are eight TMD distributions, grouped with their characteristic quark and target spin combinations (Table I). They are functions of x, Q^2 and the quark transverse momentum, $\boldsymbol{p}_T$. Three of them (the unpolarized distribution, f_1, the helicity, g_{1L}, and the transversity distributions, h_1) survive after the integration over $\boldsymbol{p}_T$, while the other five vanish. These five TMDs provide novel information on the spin-orbit correlations:

- the "Worm-gear" functions, g_{1T} and $h_{1L}^{\perp}$, describe the probability of finding a longitudinally polarized quark inside a transversely polarized nucleon and transversely polarized quark inside a longitudinally polarized nucleon, respectively. They provide important information to understand the correlations between the quark orbital an-

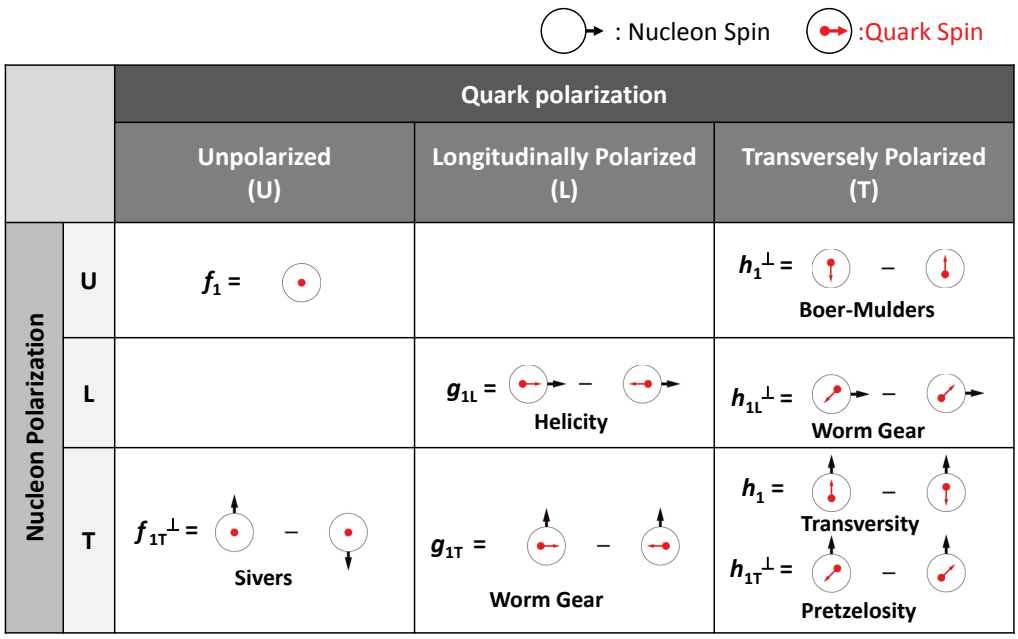

Table I: Illustration of spin correlations of all leading-twist transverse momentum distributions. The red arrows indicate spin direction of quarks; black arrows indicate spin direction of the parent nucleon. In the SIDIS process, the longitudinal direction along the virtual photon momentum transfer is horizontal in the paper.

gular momentum (OAM), the nucleon spin and the quark spin. More specific, both of the "worm-gear" functions require an interference between wave function components that differ by one unit of quark OAM, as explicitly shown in several models [3, 4, 5, 6].

- The Boer-Mulder function, $h_1^\perp$, and the Sivers function, $f_{1T}^\perp$, describe the correlations between the quark's transverse momentum and the quark spin or nucleon spin. They are T-odd TMD distributions and survive because of final state interactions (FSI) experienced by the active quark in a SIDIS experiment. They provide complementary information on the interference between wave function components that differ by one unit of OAM, as shown in the quark models [3, 4, 5, 6].

- Finally, the pretzelosity function, $h_{1T}^\perp$, involves an interference between wave function components that differ by two units of OAM (e.g. P-P or S-D interference).

Combining the wealth of information from all these TMD distributions can be invaluable for

understanding the spin-orbit correlations in the nucleon wave function and thus providing important information about the quark orbital angular momentum.

TMD distributions are mainly studied in semi-inclusive DIS (SIDIS) and hadron-hadron scatterings. In the SIDIS process, a lepton scatters off a nucleon and the leading hadrons are detected. The detected hadron carries the information of flavor and transverse momentum of the struck quark in the nucleon through a fragmentation process. The TMD distributions lead to dependencies of the SIDIS cross-section on the hadron and the target spin azimuthal angles. The SIDIS asymmetries were first observed by SMC [7], HERMES [8, 9] and CLAS [10, 11]. Further studies were performed both with transversely polarized targets by HERMES (proton) [12], COMPASS (deuteron, proton) [13, 14, 15] and Jefferson Lab Hall A (^{3}He) [16, 17], and with longitudinally polarized targets by HERMES (proton, deuteron) [18, 19], COMPASS (deuteron) [20] and CLAS (proton) [21]. Nevertheless, with the precision of the current world data, our knowledge of the TMDs is still limited. Further high statistics measurements are needed to fully understand them.

The main goal of this proposal is to provided experimental information on the neutron TMD distributions, $h_{1L}^{\perp}$, g_{1T} and g_{1L}, through the measurement of the SIDIS azimuthal asymmetries on a polarized ^{3}He target with a high statistical precision and a large kinematic coverage, which is complementary to the approved Hall A [22] and CLAS [23, 24, 25, 26, 27] TMD programs.

1.1. SIDIS Cross Section and Factorization

All eight leading-twist TMD distributions can be accessed in SIDIS. Assuming single photon exchange, the SIDIS cross section can be expressed in a model-independent way by a set of 18 Structure Functions (SF) [29] (full cross section in Appendix A). Each structure function is related to a characteristic set of a beam-target-spin combination and an azimuthal angular modulation. The following two combinations of beam-target polarization are related to the physics interests of this proposal:

- In case of an unpolarized beam, longitudinally polarized target and large azimuthal

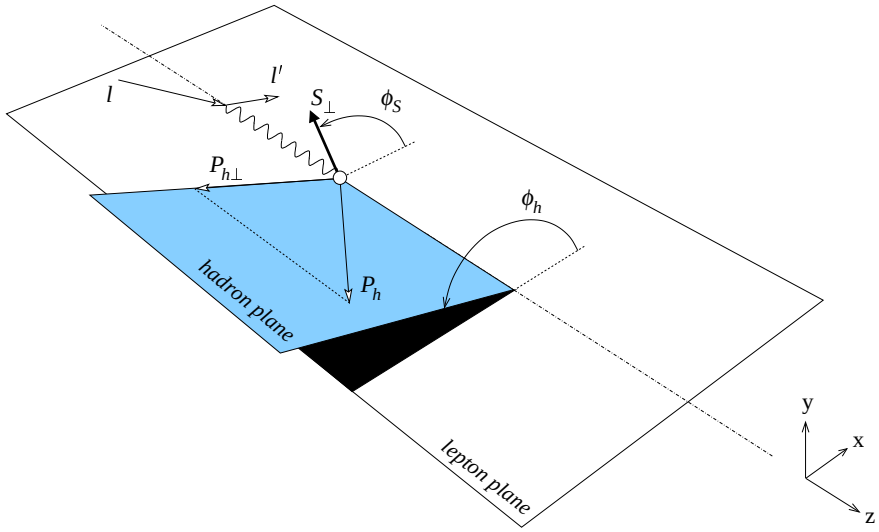

Figure 1: The Trento Conventions: Definition of azimuthal angles for SIDIS in the target rest frame [28]. $P_{h\perp}$ and $S_\perp$ are the components of P_h and S transverse to the photon momentum.

angular coverage, the related cross section can be expressed as

$$\begin{aligned} d\sigma &= d\sigma_{UU} + d\sigma_{UL} \\ &\propto F_{UU,T} + \varepsilon F_{UU,L} + S_\parallel \left(\varepsilon \sin(2\phi_h) F_{UL}^{\sin 2\phi_h} + \sqrt{2\varepsilon(1-\varepsilon)} \sin\phi_h F_{UL}^{\sin\phi_h} \right) \end{aligned} \tag{1}$$

- In case of a polarized beam, polarized target and large azimuthal angular coverage, the related cross section can be expressed as

$$\begin{aligned} d\sigma &= d\sigma_{UU} + d\sigma_{LL} + d\sigma_{LT} \\ &\propto F_{UU,T} + \varepsilon F_{UU,L} \\ &\quad + \lambda_e S_\parallel \left(\sqrt{1-\varepsilon^2} F_{LL} + \sqrt{2\,\varepsilon(1-\varepsilon)}\, \cos\phi_h\, F_{LL}^{\cos\phi_h} \right) \\ &\quad + \lambda_e\, |S_\perp| \left(\sqrt{1-\varepsilon^2} \cos(\phi_h - \phi_S) F_{LT}^{\cos(\phi_h-\phi_S)} \right. \\ &\quad \left. + \sqrt{2\,\varepsilon(1-\varepsilon)}\, \cos\phi_S\, F_{LT}^{\cos\phi_S} + \sqrt{2\,\varepsilon(1-\varepsilon)}\, \cos(2\phi_h - \phi_S)\, F_{LT}^{\cos(2\phi_h-\phi_S)} \right), \end{aligned} \tag{2}$$

where $S_\parallel$ and $S_\perp$ are longitudinal and transverse component of target spin vector, S, relative to the virtual photon direction [30], respectively. The sign convention for the longitudinal spin component is such that the target spin is parallel to the virtual photon momentum for $S_\parallel = -1$. The helicity of the lepton beam is denoted by λ_e. ϕ_h and ϕ_S are the hadron and spin azimuthal angles, respectively as defined in Figure (1) following the Trento Conventions [28]. ε is the ratio of the longitudinal and transverse photon flux, which could

be approximated as a function of y [29]. The unpolarized structure functions, $F_{UU}^{\cos\phi_h}$ and $F_{UU}^{\cos 2\phi_h}$, whose contribution will be suppressed in a spin/helicity asymmetry measurement with spin/helicity flips and a large ϕ_h coverage [105], are not listed.

At small hadron transverse momentum, $P_{h\perp}$ (defined respect to the direction of virtual photon), the structure functions are factorized as convolutions of TMD parton distribution functions (PDFs) and fragmentation functions (FFs) [29]:

$$
\begin{aligned}
F_{UU,T} &= [f_1 \otimes D_1] && (3)\\
F_{UL}^{\sin 2\phi_h} &= \left[-\frac{2(\hat{\boldsymbol{h}}\cdot\boldsymbol{k}_T)(\hat{\boldsymbol{h}}\cdot\boldsymbol{p}_T)-\boldsymbol{k}_T\cdot\boldsymbol{p}_T}{MM_h} h_{1L}^{\perp}\otimes H_1^{\perp}\right] && (4)\\
F_{LL} &= [g_{1L}\otimes D_1] && (5)\\
F_{LT}^{\cos(\phi_h-\phi_S)} &= \left[\frac{\hat{\boldsymbol{h}}\cdot\boldsymbol{p}_T}{M} g_{1T}\otimes D_1\right], && (6)\\
F_{UU,L} &= 0 && (7)\\
F_{LL}^{\cos\phi_h}, F_{LT}^{\cos\phi_S}, F_{LT}^{\cos(2\phi_h-\phi_S)} &\propto \frac{M}{Q}\ \text{(Higher twist)}, && (8)
\end{aligned}
$$

where $\hat{\boldsymbol{h}} \equiv \boldsymbol{P}_{h\perp}/|\boldsymbol{P}_{h\perp}|$, $\boldsymbol{k}_T \equiv -\boldsymbol{K}_T/z$. $\boldsymbol{K}_T$ is the transverse momentum of the leading hadron, h, with respect to the direction of the fragmenting quark. M and M_h are the mass of the nucleon and the leading hadron, respectively. The convolution notation $\big[w\, f\otimes D\big]$ is defined in Equation (A12).

1.2. Asymmetry observables

Polarized structure functions can be extracted through asymmetries, which are related to the ratios of those structure functions to $F_{UU,T}$. The asymmetries are defined so that the leading twist cross section of Equation (1) and (2) can be expressed as

$$
\begin{aligned}
d\sigma_{UU}+d\sigma_{UL} &\propto 1+S_{\parallel}\sin(2\phi_h)A_{UL}^{\sin 2\phi_h}\\
&= 1-|S|\cos\theta_S\sin(2\phi_h)A_{UL}^{\sin 2\phi_h} && (9)\\
d\sigma_{UU}+d\sigma_{LL}+d\sigma_{LT} &\propto 1+\lambda_e(S_{\parallel}A_{LL}+|S_{\perp}|\cos(\phi_h-\phi_S)A_{LT}^{\cos(\phi_h-\phi_S)})\\
&= 1+\lambda_e\,|S|\,(-\cos\theta_S A_{LL}+\sin\theta_S\cos(\phi_h-\phi_S)A_{LT}^{\cos(\phi_h-\phi_S)}), && (10)
\end{aligned}
$$

where θ_S is the polar angle of the target spin vector, S, relative to the direction of the virtual photon momentum transfer. And,

$$A_{UL}^{\sin 2\phi_h} \equiv \varepsilon \frac{F_{UL}^{\sin 2\phi_h}}{F_{UU,T}} \propto h_{1L}^{\perp} \otimes H_1^{\perp} \tag{11}$$

$$A_{LT}^{\cos(\phi_h-\phi_S)} \equiv \sqrt{1-\varepsilon^2} \frac{F_{LT}^{\cos(\phi_h-\phi_S)}}{F_{UU,T}} \propto g_{1T} \otimes D_1 \tag{12}$$

$$A_{LL} \equiv \sqrt{1-\varepsilon^2} \frac{F_{LL}}{F_{UU,T}} \propto g_{1L} \otimes D_1. \tag{13}$$

Experimentally, $A_{UL}^{\sin 2\phi_h}$ can be measured through single beam spin asymmetry with a $\sin 2\phi_h$ modulation; $A_{LT}^{\cos(\phi_h-\phi_S)}$ and A_{LL} can be measured through beam-target double spin asymmetries with angular modulations of $\cos(\phi_h - \phi_S)$ and 1, respectively. A detector with 2π azimuthal angular coverage in the lab frame gains further advantage in reducing systematic uncertainties coming from angular separations.

1.3. Overview of the Proposed Measurement

We propose a measurement of the $A_{UL}^{\sin 2\phi_h}$ and A_{LL} asymmetries in semi-inclusive electroproduction of charged pions for 35 PAC days, using the upgraded CEBAF electron beam, the Hall A polarized ^{3}He target as an effective polarized neutron target, and the newly approved SoLID spectrometer. The hardware setup is similar to that of experiment E12-10-006 [22], which measures SIDIS single target spin asymmetries with a transversely polarized ^{3}He target to study TMD PDFs of h_1, $f_{1T}^{\perp}$ and $h_{1T}^{\perp}$. In addition to the setup of E12-10-006, this measurement will use a longitudinally polarized target and a polarized beam. We also request a high beam polarization for experiment E12-10-006 to measure the $A_{LT}^{\cos(\phi_h-\phi_S)}$ asymmetry.

$A_{UL}^{\sin 2\phi_h}$ and $A_{LT}^{\cos(\phi_h-\phi_S)}$ are related to two "worm-gear" TMD PDFs of the nucleon, $h_{1L}^{\perp}$ and g_{1T} , which involve an interference between different quark orbital angular momentum states, as explicitly shown in several models [3, 4, 5, 6]. In addition, A_{LL} will constrain the flavor decomposition of quark helicity distributions of nucleons, g_{1L}, and provide information on their transverse momentum dependence.

All asymmetries will be measured with high precision and large kinematic coverages in a 4-D phase space of x, z, $P_{h\perp}$ and Q^2. The dedicated E12-10-006 data on unpolarized hydrogen and deuterium targets will be used to study the naive x-z factorization for both experiments. Systematics uncertainties are improved by the fast target spin flip. The SoLID

spectrometer provides a full coverage on the spin azimuthal angle, a large coverage in the hadron azimuthal angle, which are essential in further reducing systematic uncertainties for the extraction of different angular modulation terms. Symmetric acceptance for $\pi^{\pm}$ also reduce the uncertainties of combining $\pi^{\pm}$ asymmetries for a flavor separation.

2. PHYSICS MOTIVATION

2.1. "Worm-gear" functions, g_{1T} and $h_{1L}^{\perp}$

The main physics goal of this proposal is to provide direct experimental information for both "worm-gear" functions, g_{1T} and $h_{1L}^{\perp}$. They can be accessed through the double spin asymmetries $A_{LT}^{\cos(\phi_h-\phi_S)}$ with a transversely polarized target and the beam single spin asymmetries, $A_{UL}^{\sin 2\phi_h}$, with a longitudinally polarized target, respectively. The physics related to "worm-gear" functions, their measurement and their current experimental status will be discussed in this section.

2.1.1. "Worm-gear" functions and their relation to quark orbital motion

g_{1T} and $h_{1L}^{\perp}$ are twist-2 TMD PDFs related to the transverse motion of quark, nucleon spin and quark spin. Both of them appear at the leading-twist (twist-2) decomposition of the quark correlation functions [29, 31, 32]. More specifically, g_{1T} describes the distribution of a longitudinally polarized quark inside a transversely polarized nucleon. On the other hand, $h_{1L}^{\perp}$ describes the distribution of a transversely polarized quark inside a longitudinally polarized nucleon. They depend not only on the longitudinal momentum fraction, x, but also on the transverse momentum, $\boldsymbol{p}_T$. Since both functions link two perpendicular spin directions of nucleons and quarks, they are also known as "worm-gear" functions [33].

The spin-dependent distributions in transverse-momentum space have an analogy in terms of spin-dependent distributions in impact parameter space, described by GPDs. This correspondence hold for 6 of the leading-twist TMD PDFs, but not for the two "worm-gear" TMD PDFs because of time-reversal symmetry [34, 35, 36]. Therefore, the "worm-gear" functions can not be generated dynamically from coordinate space densities by final-state interactions. Their appearance may be seen as a genuine sign of intrinsic transverse motion of quarks [37].

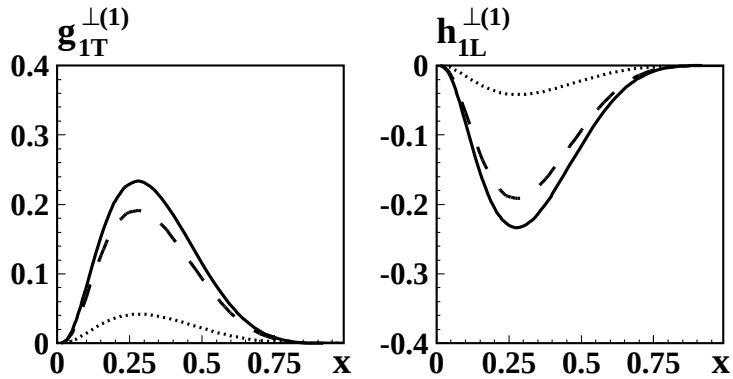

Figure 2: Flavorless $g_{1T}^{(1)}$ and $h_{1L}^{\perp(1)}$ functions (solid curves) and its component contributed from an interference between ($L = 0$, $L = 1$) (dashed curves) and an interference between ($L = 1$, $L = 2$) (dotted curves) as obtained from a light cone constituent quark model [6]. They are the integral of $g_{1T}(x, p_T)$ and $h_{1L}^{\perp}(x, p_T)$ over $\boldsymbol{p}_T$ with a weight factor of $p_T^2/2M^2$ (Equation. (A14)). The distribution functions of definite flavors follow from multiplying by factors of 4/3 for u quarks and $-1/3$ for d quarks in the proton.

Both g_{1T} and $h_{1L}^{\perp}$ are related to quark orbital motion inside nucleons. They represent the real part of an interference between nucleon wave functions that differ by one unit of orbital angular momentum, while the imaginary parts are related to the better known $f_{1T}^{\perp}$ (Sivers functions) and $h_1^{\perp}$ (Boer-Mulders functions) [3, 38]. Model studies show that g_{1T} and $h_{1L}^{\perp}$ are mainly coming from the interference between $L = 0$ and $L = 1$ states [5, 6, 39], but may also contain a small contribution from an interference between $L = 1$ and $L = 2$ states [6]. The later part is smaller than 20% over the whole x range as shown in Figure 2.

2.1.2. Lattice QCD calculations

Recent work explores TMD PDFs for the first time using lattice QCD [37, 40], so far making use of a simplified definition of TMD PDFs with straight gauge links. The "worm-gear" functions were the first spin-polarized TMD PDFs addressed with this method. They give rise to a dipole deformation of the density of quarks in the transverse momentum plane, clearly visible in Figure 4, where we show x-integrated densities obtained from lattice QCD at $m_\pi \approx 500\,\text{MeV}$. The size of the dipole deformation can be characterized by an average transverse momentum shift:

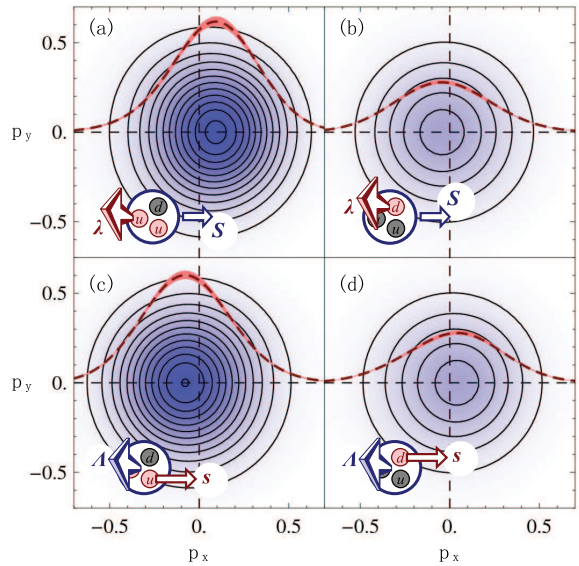

Figure 3: x-integrated quark density in the transverse momentum space, calculated using lattice QCD [37] at $m_\pi \approx 500$MeV. (a)\(b): a longitudinally ($+\boldsymbol{z}$ direction) polarized quark $u\backslash d$ density for a proton polarized in $+\boldsymbol{x}$ direction, which is related to the lowest x-moment of g_{1T}. (c)\(d): transversely ($+\boldsymbol{x}$ direction) polarized quark $u\backslash d$ density for a longitudinally ($+\boldsymbol{z}$ direction) polarized nucleon, which is related to the lowest x-moment of $h_{1L}^{\perp}$.

- In a transversely polarized nucleon for a longitudinally polarized quark (TL), the shift is

$$\langle p_x \rangle_{TL}^q = \frac{M}{n_q} \int_0^1 dx \ \left(g_{1T}^{q(1)}(x) - \bar{g}_{1T}^{q(1)}(x) \right) \tag{14}$$

  where $n_u = 2$ and $n_d = 1$ denote the number of valence quarks in the proton, and where $\bar{g}_{1T}^q$ is the anti-quark TMD PDF corresponding to g_{1T}^q. Based on a Gaussian parametrization of the transverse momentum dependence, the lattice study [40] finds $\langle p_x \rangle_{TL}^u = 69.7 \pm 4.5$ MeV and $\langle p_x \rangle_{TL}^d = -30.9 \pm 5.1$ MeV.

- In a longitudinally polarized nucleon for a transversely polarized quark (LT), the shift is

$$\langle p_x \rangle_{LT}^q = \frac{M}{n_q} \int_0^1 dx \ \left(h_{1L}^{\perp q(1)}(x) + \bar{h}_{1L}^{\perp q(1)}(x) \right) \tag{15}$$

  The lattice calculation yields $\langle p_x \rangle_{LT}^u = -59.1 \pm 3.8$ MeV and $\langle p_x \rangle_{LT}^d = 18.3 \pm 4.1$ MeV.

One finds that the u-quark has a larger shift than d-quarks with inverse sign. Also $g_{1T} \approx -h_{1L}^{\perp}$. Both of the observations support corresponding results from quark models[5, 6, 41, 42, 43, 44].

Model extractions of both $\int_0^1 dx\, g_{1T}^{(1)}(x)$ and $\int_0^1 dx\, h_{1L}^{\perp(1)}(x)$ can be significantly constrained by this proposed measurement, taking advantage of the high statistical precision and the large kinematic coverage.

2.1.3. Model Predictions

Both g_{1T} and $h_{1L}^{\perp}$ have been estimated by many quark models [5, 41, 42, 44]. Common features of these estimations suggest that g_{1T}^u is positive, g_{1T}^d is negative, and the peak amplitude of g_{1T}^u is predicted to be larger than g_{1T}^d. g_{1T} and $h_{1L}^{\perp}$ reach their maximum value in the valence quark region at a level of a few percent relative to the unpolarized distribution f_1^q.

a. Relations between g_{1T} and $h_{1L}^{\perp}$

If cylindrical symmetry around the $\boldsymbol{y}$ direction is preserved, a simple relation between two "worm-gear" functions can be concluded [35, 36], namely

$$g_{1T}^q = -h_{1L}^{\perp q}. \tag{16}$$

This relation is supported by many quark models without gluons, including a quark-model framework provided by the Bag Model [44], a Light-Cone Constituent Quark Model [5, 6], a Chiral Quark Soliton Model [36], a Spectator Model [41] and a Covariant Parton Model [43]. As discussed in Section 2.1.2, this relation is also supported by a Lattice QCD calculation to the current precisions. However, the relation does not hold in the Diquark Spectator Model discussed in Reference [39], in the quark-target model [45] and in general in QCD.

With this experiment, g_{1T} and $h_{1L}^{\perp}$ will be probed at identical kinematics with high statistical precision. A breaking of this relation would suggest the importance of quark-quark correlations and gluon contributions.

b. Predictions using the Wandzura and Wilczek (WW) Approximation + Lorentz Invariance Relations (LIRs)

One can establish, among others, the following two so-called Lorentz Invariance Relations (LIRs) [31] between p_T weighted "worm-gear" functions (Equation. (A14)) and $\boldsymbol{p}_T$ integrated twist-3 "collinear" PDFs (which, however, are not valid in general [46] and in QCD satisfied

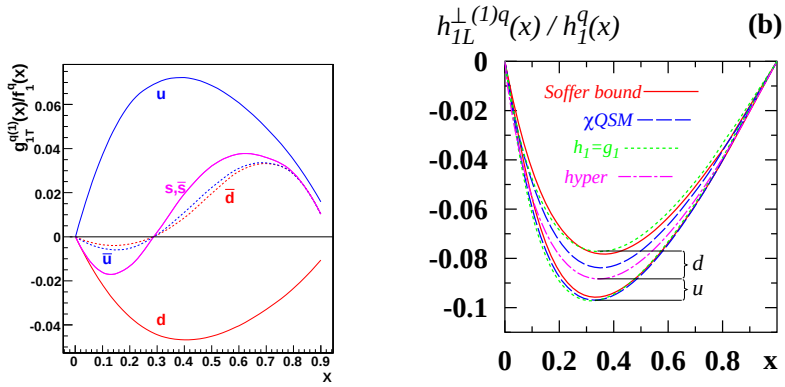

Figure 4: WW-type prediction of $g_{1T}^{q(1)}$ [42, 51, 52] (Left) and $h_{1L}^{\perp q(1)}$ [50] (right) as function of x. Notice that $g_{1T}^{q(1)}$ are plotted normalized to unpolarized PDF $f_1(x)$; $h_{1L}^{\perp q(1)}$ are plotted normalized to PDF h_1(transversity).

only in an approximation which is analog to the Wandzura-Wilczek approximation [47, 48])

$$g_T^q\ (x) = g_1^q(x) + \frac{d}{dx} g_{1T}^{q(1)}(x) \tag{17}$$

$$h_L^a\ (x) = h_1^q(x) - \frac{d}{dx} h_{1L}^{\perp q(1)}(x). \tag{18}$$

Then, using the Wandzura and Wilczek (WW) approximation [47, 49, 50]

$$g_T^q\ (x) \overset{WW}{\approx} \int_x^1 \frac{dy}{y} g_1^q(y) \tag{19}$$

$$h_L^a\ (x) \overset{WW}{\approx} 2x \int_x^1 \frac{dy}{y^2} h_1^q(y) \tag{20}$$

the "worm-gear" functions can be related to better understood collinear PDFs, g_1 and h_1:

$$g_{1T}^{q(1)}\ (x) \overset{WW-type}{\approx} x \int_x^1 \frac{dy}{y} g_1^q(y) \tag{21}$$

$$h_{1L}^{\perp q(1)}\ (x) \overset{WW-type}{\approx} -x^2 \int_x^1 \frac{dy}{y^2} h_1^q(y). \tag{22}$$

With Equations (21) and (22) [106], numerical evaluations have been performed based on experimental data of g_1 [42, 51, 52] and model predictions of h_1 [50, 53, 54]. The predictions are shown in Figure 4.

A precise extraction of g_{1T} and $h_{1L}^{\perp}$ and comparison to these calculation are highly desired, which can verify the following approximations and relations experimentally:

- WW approximation and LIRs are based on assumptions that the twist-3 "interaction dependent" terms due to quark-gluon-quark correlations and current quark mass terms are small [47, 50]. However, it was estimated that the violation on WW can be as large as $15 \sim 40\%$ [55]. This measurement is designed to provide experimental information to test this approximation.
- The calculation of h_1 can be tested through comparison with $h_{1L}^{\perp}$ indirectly.

c. More models predictions

Following models and reference papers also provided numerical evaluation of g_{1T}^{q} and/or $h_{1L}^{\perp q}$, which show similar order of magnitude as that of Figure 4:

- Diquark spectator models [4, 41, 56]
- a Light-Cone Constituent Quark Model [5, 6], also shown on Figure 2
- a covariant parton model framework with intrinsic orbital motion [43]
- a quark-model framework provided by the Bag Model [44]

2.1.4. Probing $h_{1L}^{\perp}$ and g_{1T} through SIDIS Asymmetries

$h_{1L}^{\perp}$ and g_{1T} leads to a dependence of the SIDIS cross-section on the hadron and/or target spin azimuthal angles. The dependency can be experimentally measured by the single target spin asymmetry, $A_{UL}^{\sin 2\phi_h}$, and the beam-target double spin asymmetry, $A_{LT}^{\cos(\phi_h-\phi_S)}$. They were defined in Equation (11) and (12). By substituting the structure functions defined in Equations (3) to (6), the asymmetries can be expressed without any ambiguity as

$$A_{LT}^{\cos(\phi_h-\phi_S)} = \sqrt{1-\varepsilon^2}\left[\frac{\hat{\boldsymbol{h}}\cdot\boldsymbol{p}_T}{M} g_{1T}\otimes D_1\right]\Big/[f_1\otimes D_1] \tag{23}$$

$$A_{UL}^{\sin 2\phi_h} = \varepsilon\left[-\frac{2(\hat{\boldsymbol{h}}\cdot\boldsymbol{k}_T)(\hat{\boldsymbol{h}}\cdot\boldsymbol{p}_T)-\boldsymbol{k}_T\cdot\boldsymbol{p}_T}{MM_h} h_{1L}^{\perp}\otimes H_1^{\perp}\right]\Big/[f_1\otimes D_1], \tag{24}$$

where the asymmetries are functions of $(x, y, z, P_{h\perp}, Q^2)$. The y dependency is trivial, which is only related to depolarization factor $\sqrt{1-\varepsilon^2}$ and ε. If unfavored fragmentation and sea

quark contribution is ignored, $\pi^{+(-)}$ asymmetries are directly proportional to the corresponding $u(d)$ TMD distributions.

The $P_{h\perp}$ weighted asymmetries can be defined [39, 42, 51] as

$$A_{LT}^{|P_{h\perp}|\cos(\phi_h-\phi_S)} \equiv \sqrt{1-\varepsilon^2}\frac{\int d^2\boldsymbol{P}_{h\perp}\frac{|P_{h\perp}|}{zM}F_{LT}^{\cos(\phi_h-\phi_S)}}{\int d^2\boldsymbol{P}_{h\perp}F_{UU,T}} \tag{25}$$

$$A_{UL}^{P_{h\perp}^2\sin 2\phi_h} \equiv \varepsilon\frac{\int d^2\boldsymbol{P}_{h\perp}\frac{P_{h\perp}^2}{4z^2MM_h}F_{UL}^{\sin 2\phi_h}}{\int d^2\boldsymbol{P}_{h\perp}F_{UU,T}}. \tag{26}$$

Then a simpler relation with weighted $g_{1T}^{(1)}$ and $h_{1L}^{\perp(1)}$ (Equation A14) can be expressed [39, 42, 51] as

$$A_{LT}^{|P_{h\perp}|\cos(\phi_h-\phi_S)} = 2\sqrt{1-\varepsilon^2}\frac{\sum_q e_q^2 g_{1T}^{q(1)}(x)D_1^q(z)}{\sum_q e_q^2 f_1^q(x)D_1^q(z)} \tag{27}$$

$$A_{UL}^{P_{h\perp}^2\sin 2\phi_h} \overset{TMD}{=} 2\varepsilon\frac{\sum_q e_q^2 h_{1L}^{\perp q(1)}(x)H_1^{\perp q(1)}(z)}{\sum_q e_q^2 f_1^q(x)D_1^q(z)}. \tag{28}$$

In Equation (28), TMD factorization of Equation (4) has been assumed to hold even though $A_{UL}^{P_{h\perp}^2\sin 2\phi_h}$ emphasizes high $P_{h\perp}$ region due to its weight of $P_{h\perp}^2$ (detailed discussion in [57]). Therefore, by ignoring sea quark contributions, u and d quark TMD distribution functions ($g_{1T}^{q(1)}(x)$, $h_{1L}^{\perp q(1)}(x)$) can be directly extracted with asymmetries of both $\pi^{\pm}$ (in addition to the inputs of $f_1^q(x)$ and fragmentation functions).

- For measurements with a infinite $P_{h\perp}$ coverage, this weighted asymmetry could be directly extracted from data:

$$A_{LT}^{|P_{h\perp}|\cos(\phi_h-\phi_S)} = \frac{\left\langle\frac{|P_{h\perp}|}{zM}\cos(\phi_h-\phi_S)\right\rangle_{LT}}{\langle\cos^2(\phi_h-\phi_S)\rangle_{UU}} \tag{29}$$

$$A_{UL}^{P_{h\perp}^2\sin 2\phi_h} = \frac{\left\langle\frac{P_{h\perp}^2}{4z^2MM_h}\sin 2\phi_h\right\rangle_{UL}}{\left\langle(\sin 2\phi_h)^2\right\rangle_{UU}}. \tag{30}$$

- For measurements with a finite $P_{h\perp}$ coverage, the transverse momentum dependency of TMD PDFs and FFs will became indispensable ingredient in interpreting measured asymmetries. Under an assumption of Gaussian like transverse momentum dependence, a similar relation as Equation (27) can be established between $g_{1T}(x)$ and $A_{LT}^{\cos(\phi_h-\phi_S)}$, as well as between $h_{1L}^{\perp}(x)$ and $A_{UL}^{\sin 2\phi_h}$ [42, 51, 52]. A measurement with a large coverage over $P_{h\perp}$ will also help to test and to characterize this Gaussian dependency.

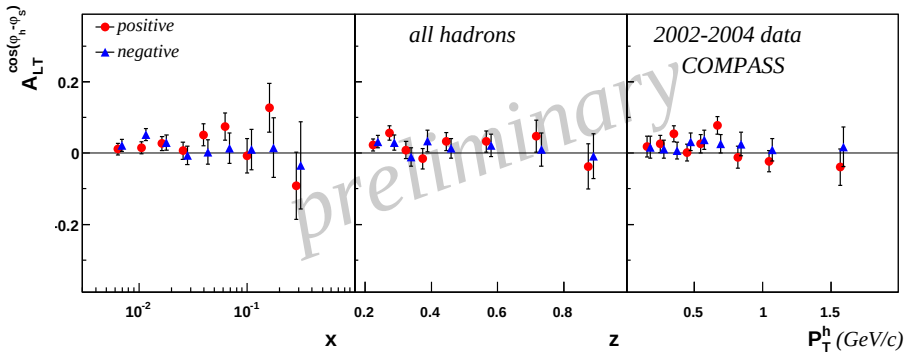

Figure 5: COMPASS measurement of $A_{LT}^{\cos(\phi_h-\phi_S)}/\sqrt{1-\varepsilon^2}$ as function of x, z and $P_{h\perp}$, using a polarized deuteron target and muon beam [58]

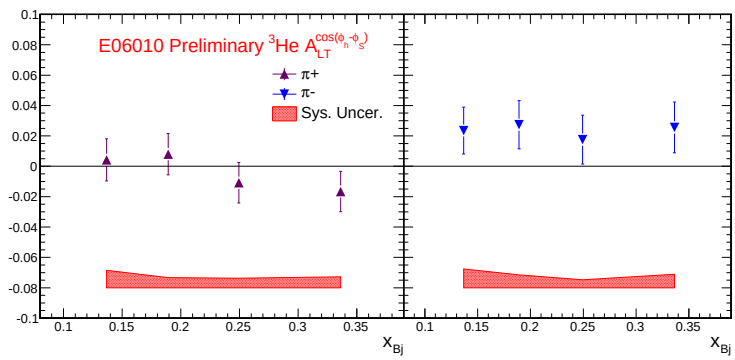

Figure 6: JLab Neutron Transversity collaboration : Preliminary results of $A_{LT}^{\cos(\phi_h-\phi_S)}$ on a polarized ^{3}He target separated into 4 x-bins. Neutron results will be generally scaled up by a proton dilution factor of ~5 (for π^+) or ~4 (for π^-) [16].

a. *Experimental Status*

There were no experimental data on $A_{LT}^{\cos(\phi_h-\phi_S)}$ and $A_{UL}^{\sin 2\phi_h}$ until recent years. Over the last decade, measurements have been made by the COMPASS collaboration [20, 58], the HERMES collaboration [9], the Jefferson Lab CLAS collaboration [59] and the Hall A Neutron Transversity Collaboration [16].

The COMPASS collaboration [58] carried out the first measurement of $A_{LT}^{\cos(\phi_h-\phi_S)}$ with a polarized muon beam on a polarized deuteron target. The results, which emphasized on the small x region (Figure 5) showed that deuteron $A_{LT}^{\cos(\phi_h-\phi_S)}$ is not significant compared to the experimental uncertainty. A new measurement has been performed by the JLab

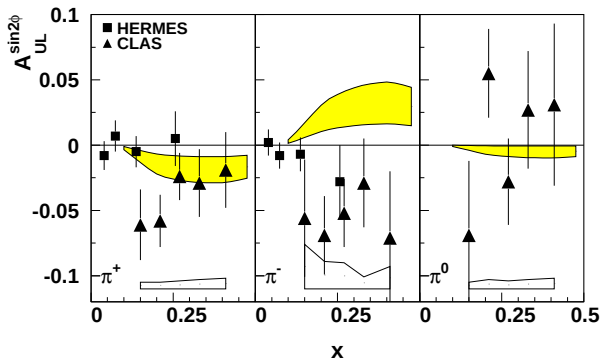

Figure 7: Proton $A_{UL}^{\sin 2\phi_h}$ as a function of x, measured by HERMES [9] (square) and JLab CLAS [59] (triangle) collaboration with systematics shown in the lower bands. Noticeably, the CLAS data show an non-zero asymmetries for both $\pi^{\pm}$ channels. The yellow band is a prediction by [50, 60] using the chiral quark-soliton model and a relation of the Wandzura–Wilczek type.

Neutron Transversity collaboration using a fast-spin-flipping electron beam (30Hz) and a transversely polarized ^{3}He target (flipped spin every 20 minute) [16]. A non-zero asymmetry was suggested by the preliminary ^{3}He $A_{LT}(\pi^-)$ results (Figure 6). However, the kinematic coverage and statistics are limited. A significant portion of the systematic uncertainty comes from the lack of information on A_{LL}, which appears as a contamination term in the A_{LT} measurement. The measurement of this proposal will benefit from both the fast beam-target spin flip to improve systematics and the larger angular coverage for minimal correlations on the modulations. Besides A_{LT} will be cleanly separated from A_{LL} with the proposed data with longitudinal-polarized ^{3}He target.

The $A_{UL}^{\sin 2\phi_h}$ asymmetry was first measured by the HERMES collaboration [9] on a polarized proton target. Deuteron data were also published in 2003 [18]. Recently, $A_{UL}^{\sin 2\phi_h}$ measurements were also published by COMPASS on a polarized deuteron target [20] and the JLab CLAS collaboration on a polarized proton target [59]. Sizable asymmetries were observed on the proton by the CLAS data (Figure 7) while the measured asymmetries for the deuteron remains small as on Figure 8. These data suggest a non-zero $A_{UL}^{\sin 2\phi_h}$ in the neutron case.

The assumption that g_{1T}^u and $h_{1L}^{\perp u}$ share opposite signs (as discussed in Section 2.1.3-a) was favored by current data under naive assumptions (the $A_{UL}^{\sin 2\phi_h}$ asymmetry for the π^+ production on a polarized proton target, as Figure 7, and the $A_{LT}^{\cos(\phi_h-\phi_S)}$ asymmetry for the

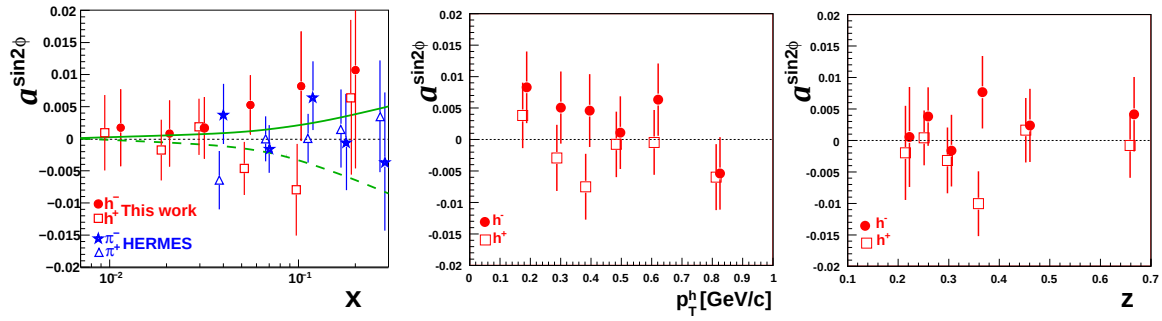

Figure 8: Deuteron $A_{UL}^{\sin 2\phi_h}$ (labeled as $a^{\sin 2\phi}$) measured by the COMPASS collaboration for all hadrons [20] (Red) and the HERMES collaboration for $\pi^{\pm}$ production [18] (Blue). Green lines are calculations by H. Avakian et al. [50] for positive (solid line) and negative (dashed line) hadrons at the HERMES kinematics.

π^- production on a polarized ^{3}He target, as Figure 6, represent the "worm-gear" functions of $h_{1L}^{\perp u}$ and g_{1T}^u, respectively).

New experiments, JLab E12-07-107 [24] and E12-09-009 [27], have been approved for measurement of $A_{UL}^{\sin 2\phi_h}$ for both pion and Kaon channels using the upgraded JLab 11 GeV polarized electron beam and the CLAS12 detector with a longitudinally polarized proton and deuteron target.

In this proposal, high precision measurements with a polarized ^{3}He target will be a complementary study to provide unique information to the "worm-gear" functions of the neutron and constrain u-d quark flavor separations.

b. Theory Parametrization

The $A_{UL}^{\sin 2\phi_h}$ and $A_{LT}^{\cos(\phi_h-\phi_S)}$ asymmetries were calculated by many models. $P_{h\perp}$ integrated asymmetries were evaluated for the kinematics of this proposal by Barbara Pasquini, et. al. [5, 6] (Figure 9), Alexei Prokudin, et. al. [42, 51, 52] and Bo-Qiang Ma, et. al. [61, 62]. These predictions are quoted on the data projections plots in Section 4.2 and Appendix B. The common features suggest that the asymmetries are at a level of a few percent; in most cases, $\pi^{\pm}$ asymmetry have opposite signs. In addition, $A_{UL}^{\sin 2\phi_h}$ and $A_{LT}^{\cos(\phi_h-\phi_S)}$ carry opposite signs due to the underlying assumed TMD relation, $g_{1T}^q = -h_{1L}^{\perp q}$.

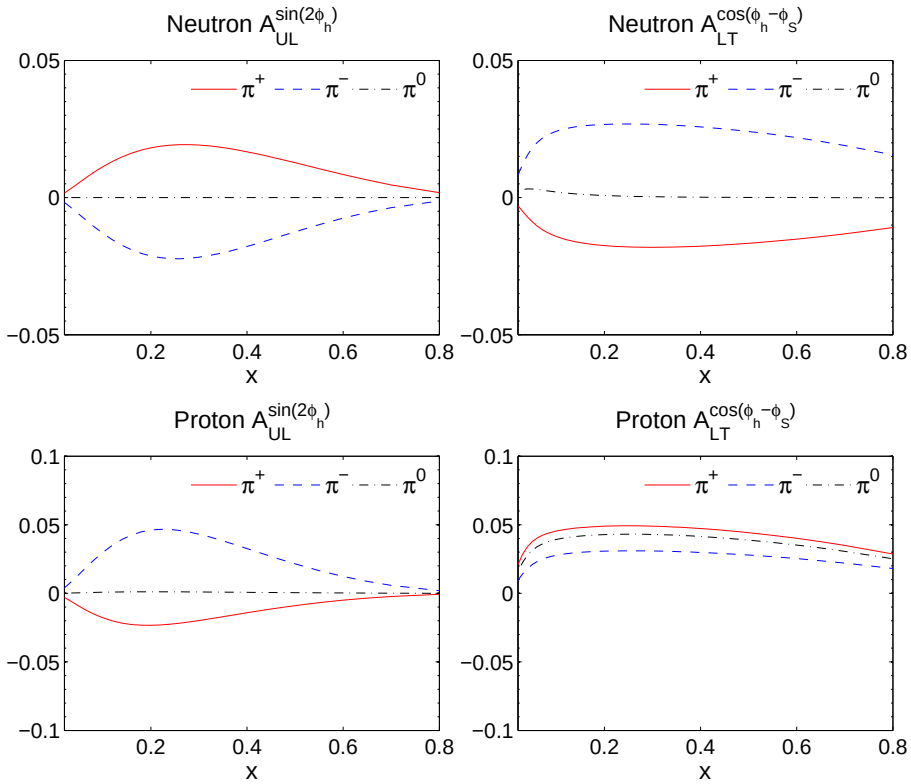

Figure 9: A prediction of $A_{UL}^{\sin 2\phi_h}$ (left) and $A_{LT}^{\cos(\phi_h-\phi_S)}$ (right) asymmetries based on a light-cone constituent quark model (LC-CQM) by Barbara Pasquini, et. al [5, 6]. The predicted asymmetries were integrated over $P_{h\perp}$ and evaluated with kinematics of this proposal and fixed $Q^2 = 2.5\,\mathrm{GeV}^2$ and $z = 0.5$. The "depolarization factor", ε (for $A_{UL}^{\sin 2\phi_h}$) and $\sqrt{1-\varepsilon^2}$ (for $A_{LT}^{\cos(\phi_h-\phi_S)}$), as in Equations (11) and (12) was not included in this calculation.

2.2. Helicity distributions, g_{1L}, with transverse momentum dependence

With a longitudinally polarized target and a polarized beam, the double spin asymmetry A_{LL} can be measured in parallel with A_{UL}. The ^{3}He A_{LL} is related to TMD helicity distribution in the neutron and is especially sensitive to the d quark with transverse momentum dependency.

2.2.1. SIDIS Study of Helicity Distribution

Quark helicity distributions, as described by spin dependent (or polarized) PDFs, carry important information of the longitudinal spin structure of nucleons. The most precise and

clearly interpreted data are from inclusive DIS experiments at CERN, SLAC, HERMES and Jefferson Lab. However, they are also limited by lacking the power of full quark flavor decomposition. Quark flavor "tagging" is significantly improved by the SIDIS process by detecting a leading hadron in fragmentation process, as well as in the hadron-hadron scatterings [1]. The existing data included HERMES (proton, deuteron, ^{3}He) [18, 19], COMPASS (deuteron) [20] and CLAS (proton) [21]. Global next-to-leading-order analysis has been performed on these data by [63, 64, 65, 66].

This proposed experiment will provide high precision data on the neutron A_{LL} asymmetry. Once included in the global analysis, this results will dramatically improve the precision of the polarized PDF of Δd.

As an illustration of the importance of this data, a leading order extraction method is discussed in this section.

a. Christova-Leader method for Flavor Separation

A global analysis of Δq can be performed with A_{LL} from multiple targets and hadrons tagged in SIDIS, as demonstrated in leading order favor decomposition with HERMES "purity method" [67]. Christova and Leader suggested a new method [68, 69, 70] by forming A_1^h, in the sum or difference of $\pi^\pm$ cross sections. For ^{3}He,

$$A_1^{\pi^+\pm\pi^-}(^3\overrightarrow{\mathrm{He}}) = \frac{1}{\sqrt{1-\varepsilon^2}}\frac{(N_{\uparrow\downarrow}^{\pi^+} - N_{\uparrow\uparrow}^{\pi^+}) \pm (N_{\uparrow\downarrow}^{\pi^-} - N_{\uparrow\uparrow}^{\pi^-})}{(N_{\uparrow\downarrow}^{\pi^+} + N_{\uparrow\uparrow}^{\pi^+}) \pm (N_{\uparrow\downarrow}^{\pi^-} + N_{\uparrow\uparrow}^{\pi^-})}. \tag{31}$$

- The $A_1^{\pi^+-\pi^-}$ asymmetries are directly related to valence quark distributions at leading order if proton polarization is ignored,

$$A_1^{\pi^+-\pi^-}(^3\overrightarrow{\mathrm{He}}) \overset{LO}{\approx} \frac{4\Delta d_v - \Delta u_v}{7f_{u_V} + 2f_{d_v}} \tag{32}$$

  In addition, this asymmetry also carries the following advantages

  - Simpler next-to-leading-order analysis due to cancellation effect on gluon terms with $\sigma(\pi^+) - \sigma(\pi^-)$
  - Contributions of diffractive ρ also cancels out in the subtraction

  By combining proton and deuteron data from CLAS [24] measurements, this experiment will improve the precision of the valence quark polarized PDF, especially on Δd_v.

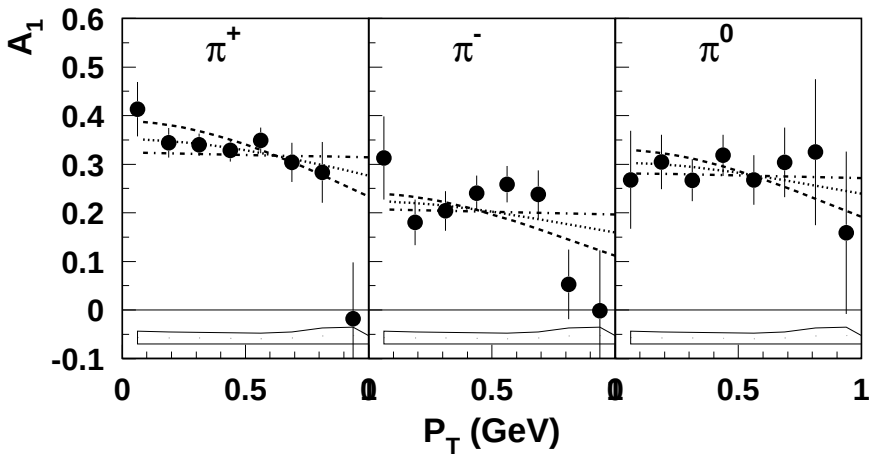

Figure 10: CLAS [59] measurement of the proton double spin asymmetry A_1 ($A_{LL}/\sqrt{1-\varepsilon^2}$ as in this document) as a function of transverse momentum $P_T = P_{h\perp}$, integrated over all kinematic variables. The open band corresponds to the systematic uncertainties. The dashed, dotted and dash-dotted curves are calculations for different ratios of transverse momentum widths for g_{1L} and f_1 (ratios=0.40, 0.68, 1.0) and a fixed width for f_1 (0.25 GeV^2) [73].

- The $A_1^{\pi^+ + \pi^-}$ asymmetries on neutron can be further used to cross-check $x - z$ factorization when compared with existing and upcoming 12 GeV high precision $A_1(\overrightarrow{n})$ data [71, 72] with the assumption that the s quark contribution can be ignored

$$A_1^{\pi^+ + \pi^-}(\overrightarrow{n}) \stackrel{LO}{=} A_1(\overrightarrow{n}) \tag{33}$$

  This check will be performed over large ranges of z, Q^2 and $P_{h\perp}$.

Besides high precision and large coverage, by detecting both $\pi^\pm$ simultaneously with nearly identical acceptance, this experiment will further suppress systematic uncertainties for the analysis with the Christova-Leader method. $(N_{\uparrow\downarrow}^{\pi^+} + N_{\uparrow\uparrow}^{\pi^+})$ is about 50% larger than $(N_{\uparrow\downarrow}^{\pi^-} + N_{\uparrow\uparrow}^{\pi^-})$ in our kinematics, which ensures enough sensitivity of this analysis by preventing Equation (31) from diverging.

2.2.2. p_T Dependence of Helicity TMD Distributions

As shown in Figure 10, there are data [59] and models [52, 73] suggesting a $P_{h\perp}$ dependence on A_{LL}. A possible interpretation of the $P_{h\perp}$-dependence of the double-spin asymmetry may involve different widths of the transverse momentum distributions of quarks with

different flavor and polarizations [73] resulting from different orbital motion of quarks polarized in the direction of the nucleon spin [74]. Clear correlations between quark helicity and transverse momentum are present in model calculations [39, 44] and lattice QCD studies [40].

This experiment will provide clean $P_{h\perp}$-dependency by the significantly improved statistics and a broad z, Q^2, x coverage.

2.3. By-products of the Proposed Measurement

This proposed experiment also provides data for exploring other physics topics, including,

- Single arm electron double spin asymmetry, A_1, which is related to quark helicity distribution.
- When combined with E12-10-006 [22] data, this experiment will provide checks of more TMD relations of
  - $g_{1L} - h_1 \stackrel{?}{=} \frac{k_\perp^2}{2M^2} h_{1T}^\perp$
  - $Df_1 + g_{1L} \stackrel{?}{=} 2h_1$
  - $2h_1 h_{1T}^\perp \stackrel{?}{=} -(g_{1L})^2$.
- By combining data of this experiment and E12-10-006, all 13 structure functions requiring a target polarization for the neutron can be disentangled. In particular, for $F_{UL}^{\sin\phi_h}$ and $F_{LL}^{\cos\phi_h}$, their physics motivation are discussed in references [18, 29, 31, 54, 73, 75].

3. PROPOSED MEASUREMENT

3.1. Experiment Setup

3.1.1. Overview

This new experiment will use the identical setup as that of experiment E12-10-006 [22], which consists of a superconducting solenoid magnet, a detector system of forward-angle detectors and large-angle detectors, and a high-pressure polarized ^{3}He target, located upstream of the magnet. In addition, high beam polarization will be requested for both experiments. The experimental layout is shown in Figure 11.

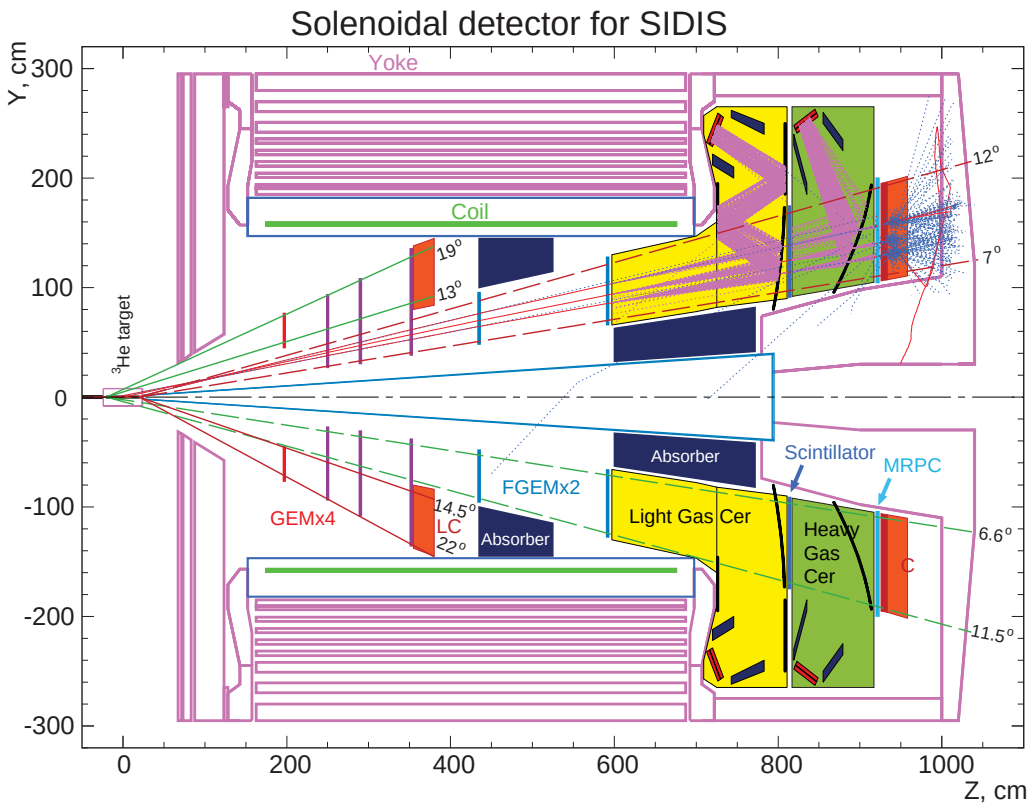

Figure 11: The experimental layout of the SoLID spectrometer based on the option of using the CDF magnet.

The acceptance is divided into large-angle and forward-angle regions. The forward angle detectors cover the polar angle from 6.6 to 12 degrees while the large angle side covers 13 to 22 degrees. Six layers of Gas Electron Multiplier (GEM) detectors will be placed inside the coils as tracking detectors for both regions. A combination of an electromagnetic calorimeter (C), gas Čerenkov counters, a layer of Multi-gap Resistive Plate Chamber (MRPC) and a thin layer of scintillator will be used for particle identification in the forward-angle region. As only electrons are designed to be clearly identified in the large-angle region, a "shashlyk"-type [76, 77] electromagnetic calorimeter (LC) will be sufficient to provide the pion rejection.

The simulation of the experiment was done with GEANT 3, details can be found in Appendix IV of proposal E12-10-006 [22]

3.1.2. CEBAF Polarized Beam

We plan to use a 15 μA beam with both 8.8 GeV and 11 GeV beam energies. A polarization of 85% is requested by this proposal. This polarization has been achieved by many JLab experiments. The beam polarization will be measured with the Hall A Møller and Compton polarimeters. In addition, the stability of the beam polarization will be continuously monitored by the Compton polarimeter.

3.1.3. Polarized ^{3}He Target

The polarized ^{3}He target is based on the technique of spin-exchange optical pumping of hybrid Rb-K alkali atoms. Such a target was used successfully in the recently completed SSA experiment [78] with a 6-GeV electron beam at JLab, achieving an in-beam polarization of 60-65%. The upstream endcap plate will keep the magnetic field and its gradients under control in the target region. In this design, the absolute magnetic field strength in the target region is about a few Gauss with field gradients < 50 mG/cm. Correction coils around the target will further reduce field gradients to the desired level of ~ 30 mG/cm. Modification of the E12-10-006 target system are needed to polarize the ^{3}He target in the longitudinal direction. Such a target system, supporting both longitudinal and transverse target directions was successfully used in a series of polarized ^{3}He experiments in Hall A, ran from 2008 to 2009 [78, 79, 80, 81].

3.1.4. Tracking

A total of six layers of GEM tracking detectors will be placed inside the magnet to determine the momentum, angle and vertex of the detected particles. The GEMs are chosen for their extraordinary performance with high rates, which have been demonstrated during the COMPASS experiment [82, 83] with a flux of 30 kHz/mm^2 which is much higher than the estimated rates in our configuration. As two of the middle layers of GEMs cover both regions, five layers of GEM detectors will be used for the forward-angle region while four layers cover the large-angle region.

With the expected GEM resolution of 200 μm, the average momentum resolution, $\delta p/p$, is about 1.2%, the polar angle resolution is around 0.3 mr, and the azimuthal angular resolution

is around 6 mr. The average vertex resolution is about 0.8 cm over the entire momentum range.

3.1.5. Electron Identification

Two sets of electromagnetic calorimeters will be used to identify electrons in the forward and large-angle regions by measuring the energy deposition in the calorimeter through an electromagnetic shower. A radiation resistant "shashlyk"-type calorimeter can be used inside the magnetic field. With a pre-shower/shower splitting, a pion rejection factor of 200:1 can be achieved at $E > 3.5$ GeV and over 100:1 at $E > 1.0$ GeV.

To further improve the electron identification in the forward-angle region, two gas Čerenkov detectors will be used. Filled with CO_2 at 1 atmospheric pressure (n=1.00045), the light gas Čerenkov has a pion momentum threshold of 4.7 GeV/c. The 2-meter long setup is expected to produce about 17 photoelectrons for high energy electrons. As the overall background is estimated to be 40 MHz in such a detector, with 30 sectors and a 20-ns coincidence window, a 40:1 pion rejection can be achieved on-line, and the off-line pion rejection can be expected to be better than 80:1.

The 80-cm long heavy gas Čerenkov detector filled with C_4F_{10} at 1.5 atmospheric pressure (n = 1.0021) will provide additional suppression for pions with momentum up to 2.2 GeV/c. With 60 MHz background and about 25 photoelectrons for electrons in the detector, the pion rejection is expected to be better than 50:1.

The E06-010 (6 GeV transversity) [78] analysis shows that by requiring coincidence between pions and electrons in the DIS region, the pion contamination can be further reduced by about a factor of 5. Assuming a similar suppression factor in the kinematics of this experiment, the pion contamination will be less than 1.5(π/e ratio)/200(Calorimeter)/5(Coincidence)$\sim$0.15% level. At forward angle, the pion contamination will be less than 100(π/e ratio)/100(Calorimeter)/80(light gas Čerenkov)/5(Coincidence)$\sim$ 0.25% level.

3.1.6. Pion Identification

For the forward-angle region, the identification of $\pi^{\pm}$ with momentum between 0.9 to 7.0 GeV/c will be one of the major goals of the SIDIS experiment. The CO_2 gas Čerenkov and heavy gas Čerenkov detectors will separate pion from heavier hadrons with momentum range of $4.7 - 16$ GeV/c and $2.2 - 7.6$ GeV/c, respectively. The background rejections are about 80:1 and 50:1 from the two detectors.

In order to identify low-momentum pions, a multi-resistive plate chamber (MRPC) detector will be inserted after the two Čherenkov detectors and before the forward-angle calorimeter. The MPRC has a typical timing resolution better than 80 ps and is not sensitive to a magnetic field. Furthermore, according to the study [84], the MRPC can work with a background rate of up to 0.28 kHz/mm^2 while the expected rate is less than 0.1 kHz/mm^2 for this proposal. With a total path length of 9 meters from the target to the MRPC plane and a conservative resolution of 100 ps, charged pions can be identified from charged kaons at a minimum rejection factor of 20:1 for a momentum range up to 2.5 GeV/c.

In conclusion, the overall contamination in the pion event sample will be controlled to less than 1% to 0.25% from high to low momenta.

3.1.7. Update of the SoLID Collaboration

Since the approval of the SoLID Transversity [22] and the SoLID PVDIS [85] proposals at PAC 35, efforts have been put both on the technical studies/simulations and on seeking contributions from international collaborations, in particular, the Chinese collaboration.

The technical progress will be in the update for the SoLID PVDIS proposal (which is up for grading) and will be presented at this PAC. With the JLab management support, the SoLID collaboration had several discussions with the Chinese collaboration, including holding a dedicated workshop in Beijing to promote the collaboration between the Chinese groups and JLab. Several Chinese institutions are interested in the collaboration, including University of Science and Technology of China (USTC), China Institute of Atomic Energy (CIAE), Huangshan University, Huazhong University of Science and Technology, Peking University, Lanzhou University, Shandong University and Tsinghua University. The Chinese collaboration plan to play a major role in the SoLID detector and the associated physics

program. The main hardware items identified to be worked on by the Chinese collaboration are the GEM detector and the MRPC. Several groups have already allocated R&D funds for these items. A major joint grant application, leading by USTC and CIAE groups, to build the GEM detector for the SoLID is being prepared and going through initial review process. The aim is to have the majority part of the GEM detector built in China. One of the main physics programs is the TMD study, including the transversity (E12-10-006 [22]) and the "worm gear" functions as proposed in this proposal.

3.2. Data Coverage and Rate Estimation

3.2.1. Data Coverage

The kinematic coverage of this proposal is identical to that of E12-10-006 [22]. The polar angle for electrons and pions coverage is from 6.6° to 22° and 6.6° to 12°, respectively. The momentum coverages for electrons and pions are from 1.0 GeV/c to 7.0 GeV/c. To ensure DIS kinematics, we will add cuts for $Q^2 > 1(\mathrm{GeV}/c)^2$, $W > 2.3$GeV and $W' > 1.6$GeV (missing mass) to avoid the resonance region. The final kinematic coverage is $x = 0.05 - 0.65$, within which $A_{UL}^{\sin 2\phi_h}$ and $A_{LT}^{\cos(\phi_h - \phi_S)}$ are predicted to reach maximum signals. By combining the data with two beam energies settings (8.8 and 11 GeV), the Q^2 range covers from $1.0 - 8.0\,(\mathrm{GeV}/c)^2$; $P_{h\perp}$ covers $0 - 1.6\,\mathrm{GeV}/c$. We choose to detect the leading pions with $0.3 < z < 0.7$ to favor the current fragmentation. The ϕ_h coverage is identical to that of experiment E12-10-006, which is improved by the large acceptance of the SoLID spectrometer. The detailed plots in bins are listed in Appendix III of [22] with more plots in reference [86]. We used a GEANT3 based simulation (appendix IV of [22]), developed by the E12-10-006 collaboration to study the correlation between phase spaces for data projections. The detailed 4-D coverage can be seen in Figures 21 and 22, as well as projection plots of Figures 15 to 20.

3.2.2. Rate Estimation

The expected rates are also identical to that of experiment E12-10-006. We have assumed a beam current of 15 μA, a target length of 40 cm with 10 amagats of ^{3}He gas, target polarization of 60% with a spin flip every 10 minutes. A GEANT3 based simulation (the

details are discussed in appendix IV of [22]) was developed by the E12-10-006 collaboration, which was used to estimate the rate at this setup. The details of material and calculated magnetic field was included in the model. A collimator has been added into the design to shield high energy electrons and photons, which are generated from the target wall in the forward-angle detector. The detector background and the momentum cut-off was studied. The overall detection efficiency is assumed to be 85% which includes the detection efficiency, computer dead time and electronic dead time. The total coincidence rates are 1.7 kHz (π^+) and 1.1 kHz (π^-) with the 11 GeV beam, 0.93 kHz (π^+) and 0.63 kHz (π^-) with the 8.8 GeV beam. A complete list of rates is included in Section 10 of [22].

3.3. Data Analysis Strategies

Data will be analyzed with the following procedures:

1. Data from both beam energies will be combined and binned with 6 bins in Q^2 and 8 bins in z. For each Q^2 and z bin, data will be further separated into $P_{h\perp}$ bins (every 0.2MeV) and x bins depending on the statistics. The total bin number will be more than 1400.

2. For each bin, the ^{3}He angular modulation asymmetries will be extracted according to the definitions of Equation (11) to (13). Two methods have been developed by the 6 GeV Neutron Transversity Collaboration to extract angular modulated asymmetries with target spin flips, charge life time correction and imperfect acceptance. Both of them can be directly applied to the analysis of this experiment

   (a) The Maximum Likelihood Method [87], which directly extract the angular modulated asymmetries on the $(\theta_S, \phi_S, \phi_h)$ phase space, with the corrections on the biases from luminosity, DAQ live time and partial acceptance.

   (b) The angular binning and fitting method [88], which can be further developed into a form to further cancel out systematic uncertainties as in [22].

   A small contribution of events from N_2 gas inside the target cell, which do not carry any target spin related asymmetries, will dilute the measured asymmetry by about 10%. The dilution correction will be directly related to ^{3}He-N_2 relative cross sections,

which will be precisely measured by dedicated N_2 and ^{3}He reference cell runs, a well established procedure for the polarized ^{3}He programs at Jefferson Lab [88].

3. Extraction of neutron asymmetries: ^{3}He asymmetries are related to that of neutron through effective nucleon polarization in ^{3}He for DIS

$$A^{^3\mathrm{He}} = \frac{A^n P^n \sigma^n + 2A^p P^p \sigma^p}{\sigma^n + 2\sigma^p} \tag{34}$$

or

$$A^n = \frac{1}{f^p P^n}\left(A^{^3\mathrm{He}} - (1 - f^p)\, A^p P^p\right) \tag{35}$$

where the proton dilution factor $f^p \equiv \sigma^n/(\sigma^n + 2\sigma^p)$, which is only related to relative proton-neutron cross sections σ^p/σ^n will be precisely measured through H_2, D_2 and ^{3}He reference cell data. The effective polarizations, based on global analysis of nuclear models [72, 89, 90, 91, 92], are

$$P^n = 0.86^{+0.036}_{-0.02} \tag{36}$$

$$P^p = -0.028^{+0.009}_{-0.004} \tag{37}$$

The proton asymmetry can be estimated through current and future measurements of [1, 9, 24, 58, 59]. The uncertainty introduced by this method are discussed in Section 4.2.

4. RESULTS AND PROJECTIONS

4.1. Beam time and statistical uncertainty estimations

4.1.1. Beam polarization and time

We request 35 days of total beam time to match about 50% statistics of experiment E12-10-006 [22]. The detailed beam time is shown in Table II. The beam are requested to be 15uA with 85% polarization. When combined with experiment E12-10-006, this experiment will not require any beam time for calibration data, including reference cell runs and detector calibrations. We also request beam polarization for E12-10-006 to be 85% to produce high precision data on $A_{LT}^{\cos(\phi_h - \phi_S)}$.

	Time (hour)	Time (day)
Production on longitudinally polarized ^{3}He with 11 GeV beam	538	22.5
Production on longitudinally polarized ^{3}He with 8.8 GeV beam	228	9.5
Target Overhead (polarimetry, spin flips, etc.)	60	2.5
Total	**826**	**34.5**

Table II: Beam time request for longitudinal target running

4.1.2. Statistical uncertainty estimation

With 35 PAC days of longitudinal data, the statistical precision of $A_{UL}^{\sin 2\phi_h}$ and A_{LL} will reach the same level of the SSA measurements in E12-10-006 [22]. In addition, $A_{LT}^{\cos(\phi_h-\phi_S)}$ can be cleanly disentangled from A_{LL} by combining both the transverse and longitudinal target spin data.

A simulation was performed with 35 PAC days of data with a longitudinal target polarization. A maximum likelihood method [87] was used to extract angular modulations with a combined data set from both this measurement and E12-10-006. Data were binned into 4-dimensional $(x, P_{h\perp}, z, Q^2)$ bins. For a typical z and Q^2 bin ($0.40 < z < 0.45$, $2\,\mathrm{GeV}^2 < Q^2 < 3\,\mathrm{GeV}^2$, one of the total 48 z-Q^2 bins), data projections are shown in Figures 12, 13 and 14, for $A_{UL}^{\sin 2\phi_h}$, $A_{LT}^{\cos(\phi_h-\phi_S)}$ and A_{LL}, respectively. The center of each red point corresponds to the kinematics center of each x and $P_{h\perp}$ bin and the error bar corresponds to the statistical uncertainty of the asymmetry for each 4-dimensional $(x, P_{h\perp}, z, Q^2)$ bin. The scale of the asymmetries and uncertainties is shown on the right side axis. In addition, projections of all 48 z and Q^2 bins are plotted with the same legend in Appendix B, Figures 15 to 20. In addition to projections, following curves and data are also plotted:

- The theoretical predictions of $A_{UL}^{\sin 2\phi_h}$ and $A_{LT}^{\cos(\phi_h-\phi_S)}$ are based on the calculation of Barbara Pasquini, et. al [5, 6] (blue solid lines, shown separately in Figure 9), Bo-Qiang Ma, et. al. [61, 62] (black solid and dash curves represent two approaches of parametrizations) and Alexei Prokudin, et. al. [42, 51, 52] (magenta dash-dot curve). The predicted asymmetries were integrated over $P_{h\perp}$, which represent the average size of the asymmetries in $P_{h\perp}$ bins.

- Preliminary uncertainties of the E06-010 [16] results are also shown with $A_{LT}^{\cos(\phi_h-\phi_S)}$

projections as a comparison with the current precision of the neutron (^{3}He) measurements.

- A next-to-leading order (NLO) analysis of world data [107] was used to predict $P_{h\perp}$ integrated A_{LL} as shown in Figures 14, 19 and 20.

4.2. Systematic Uncertainty Estimation

The systematic uncertainties for the neutron asymmetries are estimated in this section.

4.2.1. Raw Azimuthal Asymmetry

The azimuthal asymmetry observables will be directly reconstructed over angular phase space with the maximum likelihood method [87]. A simplified expression can be expressed as

$$A^W_{Asym} = \frac{< Sign_{Asym} \cdot P_{Asym} \cdot W >}{< P^2 W^2 >} + \mathcal{O}(A_{\text{Lumi},Asym} A^W_{\text{Accep}}), \tag{38}$$

where A^W_{Asym} is azimuthal asymmetry with angular modulation of $W(\theta_S, \phi_h, \phi_S)$. Subscript $Asym$ stand for target spin asymmetry for A_{UL} and $Sign_{Asym} = 1$; It stands for beam spin asymmetry for A_{LL}, A_{LT} and $Sign_{Asym}$ is the sign of beam helicity (It is also possible to form target spin asymmetry to extract A_{LL}, A_{LT} as [20, 58]. However systematic uncertainties are significantly improved for Jefferson Lab experiments by forming the beam spin asymmetries, taking the advantage of the fast CEBAF helicity flips). P is the product polarizations: $P_{Asym} = P_{\text{Target}}$ for A_{UL} or $P_{Asym} = P_{\text{Beam}} \cdot P_{\text{Target}}$ for A_{LL} and A_{LT}. $< X >$ stand for the sum over the whole data set of a function X, which is evaluated at each event. The leading correction term is proportional to the product of two asymmetries, $A_{\text{Lumi},Asym} A^W_{\text{Accep}}$: $A_{\text{Lumi},Asym}$ is the luminosity asymmetry between two spin states of beam or target, which will be controlled to be small by balancing beam charge in each spin state and a large number of spin flips; A^W_{Accep} is the acceptance asymmetry with modulation W for a single spin state, which is an integration of W over the phase space.

Therefore, systematic uncertainties on the azimuthal asymmetry extraction include the following contributions: angular reconstruction, polarimetry, normalization errors and the detector efficiency drift.

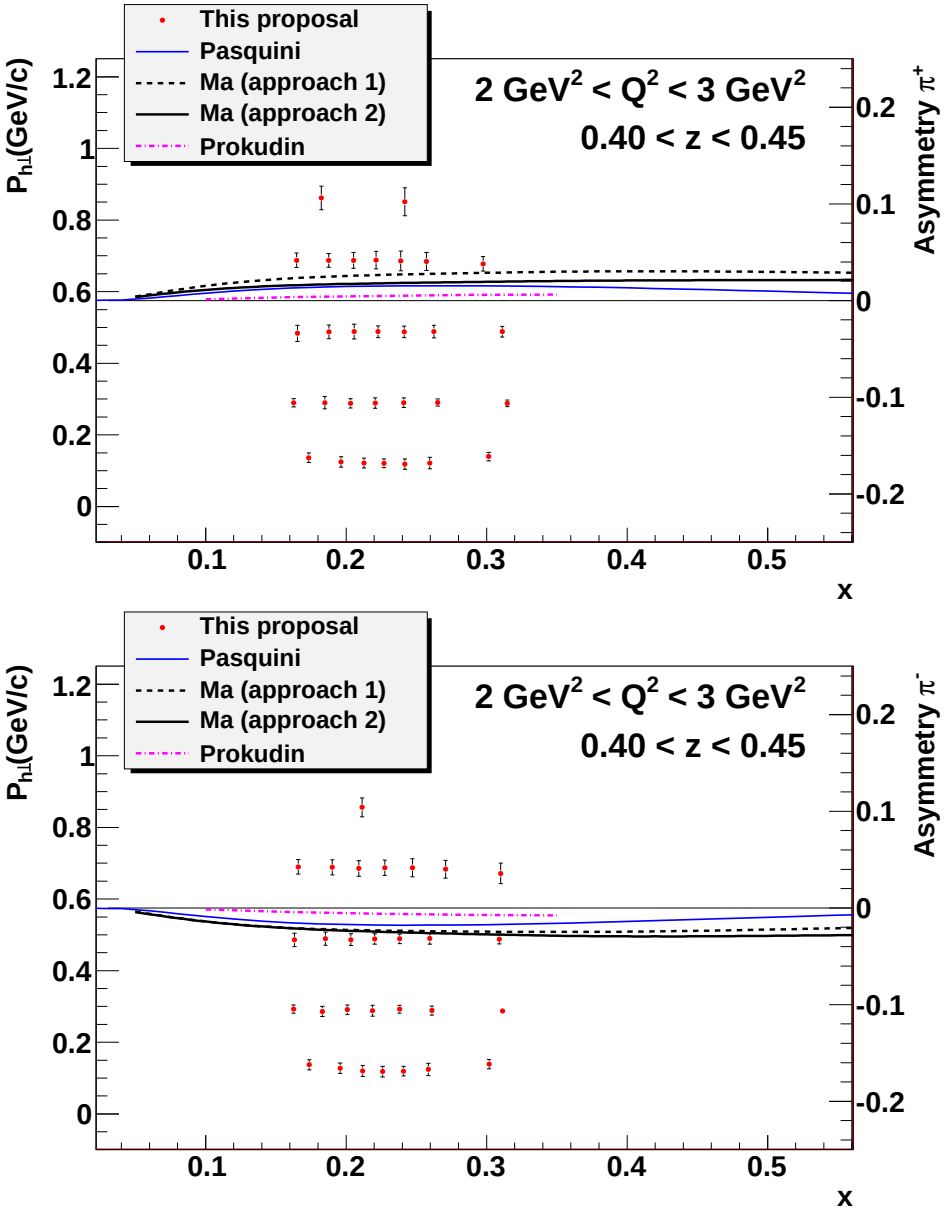

Figure 12: Projections of $A_{UL}^{\sin 2\phi_h}$ for coincidence $e'\pi^+$ channel (upper plot) and $e'\pi^-$ channel (lower plot) in a single z and Q^2 bin ($0.40 < z < 0.45$, $2\,\mathrm{GeV}^2 < Q^2 < 3\,\mathrm{GeV}^2$). The **blue curve** is predicted asymmetry with a light-cone constituent quark models, evaluated at $Q^2 = 2.5\,\mathrm{GeV}^2$ and $z = 0.5$ by Barbara Pasquini, et. al [5, 6]; the **black curves** (solid and dash represent two approaches of parametrizations) are predicted asymmetries with a light-cone quark-diquark model with the Melosh-Wigner rotation effect [93, 94] taken into account, calculated by Bo-Qiang Ma, et. al. [61, 62]; The **magenta dash-dot curve** is prediction based on the WW-type relations by Alexei Prokudin, et. al. [42, 51, 52]. All theory predictions are integrated over $P_{h\perp}$.

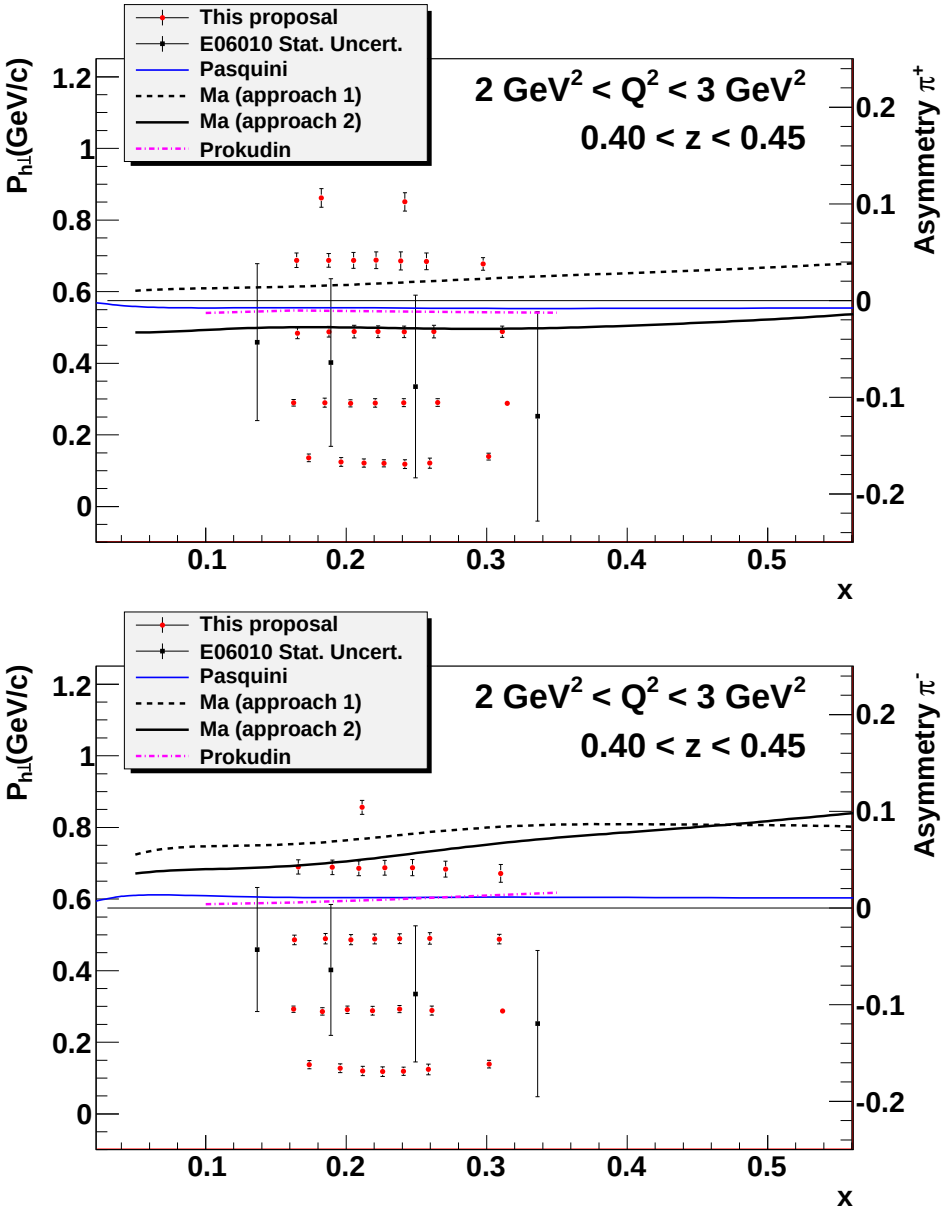

Figure 13: Projections of $A_{LT}^{\cos(\phi_h-\phi_S)}$ for coincidence $e'\pi^+$ channel (upper plot) and $e'\pi^-$ channel (lower plot) in a single z and Q^2 bin ($0.40 < z < 0.45$, $2\,\mathrm{GeV}^2 < Q^2 < 3\,\mathrm{GeV}^2$). The **blue curve** was predicted asymmetries with a light-cone constituent quark models, evaluated at $Q^2 = 2.5\,\mathrm{GeV}^2$ and $z = 0.5$ by Barbara Pasquini, et. al [5, 6]; the **black curves** (solid and dash represent two approaches of parametrizations) are predicted asymmetries with a light-cone quark-diquark model with the Melosh-Wigner rotation effect [93, 94] taken into account, calculated by Bo-Qiang Ma, et. al. [61, 62]; The **magenta dash-dot curve** is prediction based on the WW-type relations by Alexei Prokudin, et. al. [42, 51, 52]. All theory predictions are integrated over $P_{h\perp}$. The **black data points** are preliminary statistical uncertainties of E06-010 data. The (x, y) coordinate of the E06-010 data are at kinematic center of $(x, P_{h\perp})$.

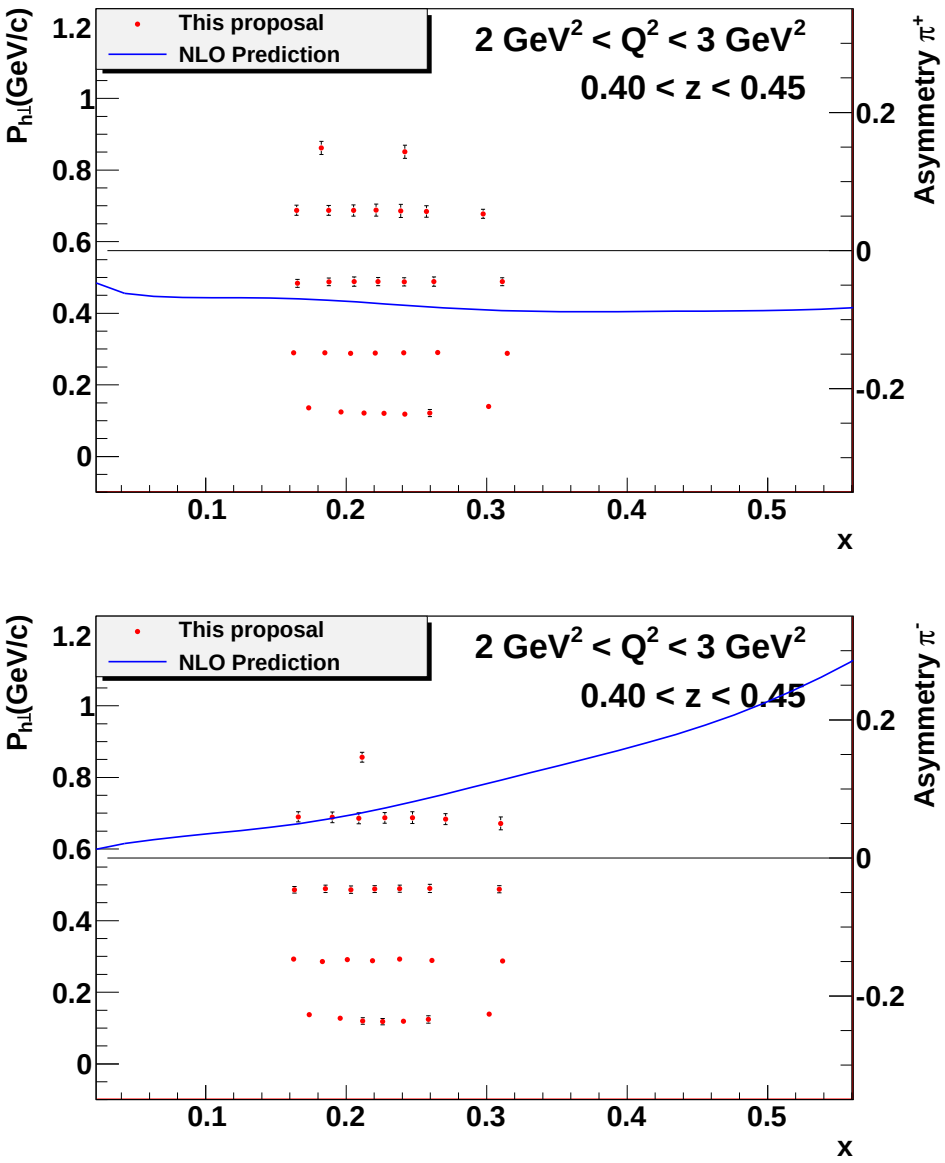

Figure 14: Projections of A_{LL}, for coincidence $e'\pi^+$ channel (upper plot) and $e'\pi^-$ channel (lower plot) in a single z and Q^2 bin ($0.40 < z < 0.45$, $2\,\mathrm{GeV}^2 < Q^2 < 3\,\mathrm{GeV}^2$). The blue lines are $P_{h\perp}$ integrated A_{LL} prediction at $Q^2 = 2.0\,\mathrm{GeV}^2$ and $z = 0.425$, based on the next-to-leading order (NLO) parametrization of unpolarized PDF [95], polarized PDF [96] and unpolarized FF [97].

a. Angular Reconstruction Errors

- A_{LL} measurement do not require knowledge of angular modulations
- Uncertainties on the azimuthal angle (ϕ_h, ϕ_S) reconstructions contribute to angular modulation measurements of $A_{UL}^{\sin 2\phi_h}$ and $A_{LT}^{\cos(\phi_h-\phi_S)}$. There are two category of un-

certainties:

- Statistical uncertainties due to tracking precision and random background: It was demonstrated that the statistical fluctuation of ϕ_h reconstruction is less than 2° as shown on Figure. 16 of [22]. The fluctuation on the ϕ_S reconstruction is better, since it only involve the fluctuations on the electron azimuthal angle reconstruction at the leading order. Following Equation. (38), the random fluctuation will cancel out at leading order during sum over events. The residue effect is suppressed by $1/\sqrt{N_{\text{event}}}$ and become negligible.
- The systematical shifts during angular reconstruction, which include two contributions: optics angular calibration uncertainty of the SoLID spectrometer, which was estimated around 0.2° with sieve calibration, and precision of was target spin angle, which was also around 0.2° based on the precision of the target holding field measurement. Therefore, the total shift uncertainties on both ϕ_h and ϕ_S are around $\sqrt{2} \times 0.2^\circ \approx 0.3^\circ$.
  - For the angular modulation measurement of $\cos(\phi_h - \phi_S)$ for A_{LT}, the $\phi_h - \phi_S$ coverage is symmetric and complete. The shift contribute to the measurement as 2nd order dilution, which is estimated by $\left[\Delta\left(\phi_h - \phi_S\right)\right]^2 \sim 5 \times 10^{-5}$. It corresponds to the neutron asymmetries to the level of 3×10^{-4} (relative).
  - For angular modulation measurement of $\sin 2\phi_h$ for A_{UL}, the shift contribute at 1st order shift at the worse possible cases of partial ϕ_h coverages. Fortunately, for the final target asymmetry measurement with fast target spin flips, the systematic uncertainty on angular modulation was canceled out to the first order and suppressed by the target spin related luminosity asymmetry. Therefore, the total contribution is on the level of $\Delta\phi_h \times A_{\text{Lumi},Spin} \sim 3.5 mrad \times 10\%(\text{max } A_{\text{Lumi}} \text{ for a 20 min spin pair}) \div \sqrt{2300(\#\text{ spin flips})} \sim 7ppm$ (absolute).

In conclusion, the systematic uncertainties due to angular reconstruction errors are negligible.

b. Polarimetry Errors

The relative uncertainties on polarimetry are 3% for both target [108] and beam polarization, respectively. This gives a 3% (relative) uncertainty to A_{UL} measurements and a 4% (relative) uncertainty to both A_{LL} and A_{LT}.

c. Normalization Errors

Normalization errors, which are related to luminosity and acceptance, correspond to correction terms of $\mathcal{O}(A_{\mathrm{Lumi},Asym}A^{W}_{\mathrm{Accep}})$. For this A_{LL} measurement, $A^{W}_{\mathrm{Accep}} = A^{-\cos\theta_S}_{\mathrm{Accep}}$ is suppressed due to the target spin flips; for the $A_{LT}^{\cos(\phi_h-\phi_S)}$ case, $A^{\sin\theta_S\cos(\phi_h-\phi_S)}_{\mathrm{Accep}}$ is suppressed due to the double cancellation of the (rotational) symmetric coverage of ϕ_S and the target spin flips. For $A_{UL}^{\sin 2\phi_h}$, $A^{W}_{\mathrm{Accep}} = A^{-\cos\theta_S\sin 2\phi_h}_{\mathrm{Accep}}$ is suppressed by (reflectional) symmetric coverage of ϕ_h. There are triple systematics cancellation effects for the $A_{LT}^{\cos(\phi_h-\phi_S)}$ measurement (double spin flip+symmetric angular coverage); double cancellation for the A_{LL} measurement (double spin flip); and double cancellation effects for the $A_{UL}^{\sin 2\phi_h}$ measurement (target spin flip + symmetric coverage of ϕ_h).

d. Detector efficiency drift

- $A_{UL}^{\sin 2\phi_h}$: the uncertainty due to the time dependent drift of detector efficiency drift is suppressed by the fast target spin flips. Target spin flips ever 10 min, for total 32 days of production running, resulting $\sim$ 2300 spin pairs. With in a 10 min spin state, the detector efficiency will be monitored to a precision of 1% by single electron/pion rate. The systematic uncertainty due to the detector efficiency drift is $1\%/\sqrt{2300} \approx 2\times10^{-4}$, which translate into neutron physics asymmetry of $\sim 1\times10^{-3}$ (absolute).

- $A_{LT}^{\cos(\phi_h-\phi_S)}$ and A_{LL}: such a systematic uncertainty is further suppressed by flipping beam helicity at 30Hz. The efficiency drift is negligible for this proposed measurement.

4.2.2. Random Coincidence

With a 6 ns coincidence window [109], the average random coincidence background is 2% for both $\pi^{\pm}$ channels. The background will be further suppressed by a factor of 4 due to vertex coincidence [110]. On average less than a 0.5% (relative) systematic uncertainty from

the background. In the worst case scenario, such as at high $P_{h\perp}$ bins, the signal-to-noise ratio is about 5.

4.2.3. Cross Talk Between Asymmetries

The asymmetries produced in Section 4.1.2 are fitted with all leading-twist asymmetries. The longitudinal and transverse spin components are cleanly separated by combining data with both spin directions.

The high-twist terms will be another source of the systematic uncertainties. Those terms are modulated by different azimuthal angular functions than the leading twist ones. Size of the high-twist terms can be directly measured by including them in the fitting procedure. The cross talk between angular modulations is suppressed with the large azimuthal angle acceptance provided by the SoLID spectrometer.

4.2.4. Nuclear Effects of ^{3}He

The ^{3}He to neutron extraction was discussed in Section 3.3. There is a small offset due to the proton effective polarization (-2.8%). The proton asymmetry can be estimated from the measurements of [1, 9, 24, 58, 59]. The uncertainty of the proton polarization is estimated at 0.7%(uncertainty on proton polarization) $\times$ 2(max asymmetry ratio) $\times$ 3(max cross section ratio, $2\sigma_p/\sigma_n$) = 4.2% (relative). Data with large kinematic coverage from this experiment will also help understand ^{3}He nuclear system.

4.2.5. Test of Factorization

The universality of the quark and gluon distribution and fragmentation functions and their scale dependence are implied by the existence of QCD factorization theorems. A factorization theorem for SIDIS with $P_{h\perp} \ll Q$ was argued by theory work of [98, 99]. The validity of leading order x-z factorization were also tested experimentally by the HERMES [100], Jefferson Lab Hall C [22] and Hall B [101] collaborations. For kinematics of this experiment, we plan to use the dedicated E12-10-006 data on unpolarized hydrogen and deuterium targets [22] to further test the naive x-z factorization.

4.2.6. Target Fragmentation

We cut on $z > 0.3$ to avoid the target fragmentation region. A Study [102] based on HERMES LUND fragmentation parametrization [103] suggested that the target fragmentation contamination is small at the coverage of z of this experiment ($0.3 < z < 0.7$, after kinematics cuts for SIDIS asymmetry measurements). Further studies can be performed with the expected data sets of both this experiment and E12-10-006, taking advantage of the large z coverage (which extends to larger than $0.3 < z < 0.7$).

4.2.7. Diffractive Vector Meson Production

The diffractive vector meson contamination is expected to be the same as that of E12-10-006, as discussed in [22] for the identical kinematics. The contribution of the pions from the decay of the diffractive production is estimated based on the HERMES tuned Pythia simulation. The average contamination from the diffractive production on neutron is about 7% and 8% for π^+ and π^-, respectively (shown in Figure 23). The correction is treated as a dilution effect. Assuming a 30% relative uncertainty on the diffractive cross section estimation based on Pythia, a 3% (relative) uncertainty is contributed by this contamination.

4.2.8. Radiative Correction

The radiative correction was studied at the same kinematics in [102], which indicated that the kinematic smearing effect is less than 20%. The effect for double spin asymmetry cases was suggested to be small ($\sim 1\%$) in reference [**104**]. The contamination from exclusive channels is less than 3%. In addition, the low W data taken by this experiment will help study the exclusive asymmetries and reduce the systematic uncertainty.

4.2.9. Systematic Uncertainty Budget

Table III summarizes the budget for the systematic uncertainties, which is much smaller than the statistical uncertainties.

Source	Type	$A_{UL}^{\sin 2\phi_h}$	$A_{LT}^{\cos(\phi_h-\phi_S)}$	A_{LL}
Raw Asymmetries	absolute	1×10^{-3}	negligible	negligible
Random Coinc. Background Subtraction	relative	1%	1%	1%
polarimetry	relative	3%	4%	4%
Nuclear Effects	relative	4%	4%	4%
Diffractive Vector Meson	relative	3%	3%	3%
Radiative Corrections	relative	2%	3%	3%
Total	**absolute**	1×10^{-3}	negligible	negligible
	relative	7%	7%	7%
Stat. Uncertainty for a Typical Bin	absolute	5×10^{-3}	4×10^{-3}	4×10^{-3}

Table III: Budget for systematic uncertainties. Statistical uncertainty for a typical bin are shown on the last row, which are plotted in Figure 15 to 20.

5. SUMMARY

We propose a measurement of the neutron azimuthal asymmetries of $A_{UL}^{\sin 2\phi_h}$ and A_{LL} in semi-inclusive electroproduction of charged pions for 35 PAC days, using the upgraded CEBAF electron beam, the Hall A polarized ^{3}He target and the newly approved SoLID spectrometer. In addition, high beam polarization is requested to measure a beam-target double spin asymmetry, $A_{LT}^{\cos(\phi_h-\phi_S)}$.

The $A_{UL}^{\sin 2\phi_h}$ and $A_{LT}^{\cos(\phi_h-\phi_S)}$ asymmetries are related to two "worm-gear" TMD distributions of nucleons, $h_{1L}^{\perp}$ and g_{1T}, which provide important information to understand the correlations between the quark orbital angular momentum (OAM), the nucleon spin and the quark spin. High precision, 4-D (x, z, $P_{h\perp}$, Q^2) data will expand our knowledge of the nucleon spin structure in terms of the orbital motions of underlying quarks and gluons described by the QCD dynamics. In addition, A_{LL} data will improve the precision of global analysis on helicity distributions in nucleon, especially for the d quark.

The measurement shares the setup with experiment E12-10-006 [22] with additional requirements of a longitudinally polarized target and a polarized beam. Active efforts has been put both on the technical studies/simulations and on seeking contributions from international collaborations. Encouraging responds have been received. Together, these two

SoLID TMD experiments will define the precision of world data of SIDIS on an effective polarized neutron target.

Appendix A: FULL SIDIS CROSS SECTION AT SMALL TRANSVERSE MOMENTUM

Assuming single photon exchange, the lepton-hadron cross section can be expressed in a model-independent way by a set of structure functions. We follow the notation of reference [29] that,

$$
\begin{aligned}
\frac{d\sigma}{dx\,dy\,d\psi\,dz\,d\phi_h\,dP_{h\perp}^2} \;=\; & \frac{\alpha^2}{xyQ^2}\,\frac{y^2}{2\,(1-\varepsilon)}\left(1+\frac{\gamma^2}{2x}\right)\times \\
& \Bigg\{F_{UU,T}+\varepsilon\,F_{UU,L}+\sqrt{2\,\varepsilon(1+\varepsilon)}\,\cos\phi_h\,F_{UU}^{\cos\phi_h} \\
& +\varepsilon\cos(2\phi_h)\,F_{UU}^{\cos 2\phi_h}+\lambda_e\,\sqrt{2\,\varepsilon(1-\varepsilon)}\,\sin\phi_h\,F_{LU}^{\sin\phi_h} \\
& +S_\parallel\left[\sqrt{2\,\varepsilon(1+\varepsilon)}\,\sin\phi_h\,F_{UL}^{\sin\phi_h}+\varepsilon\sin(2\phi_h)\,F_{UL}^{\sin 2\phi_h}\right] \\
& +S_\parallel\lambda_e\left[\sqrt{1-\varepsilon^2}\,F_{LL}+\sqrt{2\,\varepsilon(1-\varepsilon)}\,\cos\phi_h\,F_{LL}^{\cos\phi_h}\right] \\
& +|\boldsymbol{S}_\perp|\Bigg[\sin(\phi_h-\phi_S)\left(F_{UT,T}^{\sin(\phi_h-\phi_S)}+\varepsilon\,F_{UT,L}^{\sin(\phi_h-\phi_S)}\right) \\
& +\varepsilon\,\sin(\phi_h+\phi_S)\,F_{UT}^{\sin(\phi_h+\phi_S)}+\varepsilon\,\sin(3\phi_h-\phi_S)\,F_{UT}^{\sin(3\phi_h-\phi_S)} \\
& +\sqrt{2\,\varepsilon(1+\varepsilon)}\,\sin\phi_S\,F_{UT}^{\sin\phi_S}+\sqrt{2\,\varepsilon(1+\varepsilon)}\,\sin(2\phi_h-\phi_S)\,F_{UT}^{\sin(2\phi_h-\phi_S)}\Bigg] \\
& +|\boldsymbol{S}_\perp|\lambda_e\Bigg[\sqrt{1-\varepsilon^2}\,\cos(\phi_h-\phi_S)\,F_{LT}^{\cos(\phi_h-\phi_S)}+\sqrt{2\,\varepsilon(1-\varepsilon)}\,\cos\phi_S\,F_{LT}^{\cos\phi_S} \\
& +\sqrt{2\,\varepsilon(1-\varepsilon)}\,\cos(2\phi_h-\phi_S)\,F_{LT}^{\cos(2\phi_h-\phi_S)}\Bigg]\Bigg\}
\end{aligned}
\tag{A1}
$$

For low transverse momentum of the detected hadron, the structure functions were calculated at tree level in terms of transverse-momentum-dependent parton distribution and fragmentation functions [29]. The result on leading twist structure functions are quoted

below.

$$F_{UU,T} = \left[f_1 \otimes D_1\right] \tag{A2}$$

$$F_{UU,L} = 0 \tag{A3}$$

$$F_{UU}^{\cos 2\phi_h} = \left[-\frac{2\left(\hat{\boldsymbol{h}}\cdot\boldsymbol{k}_T\right)\left(\hat{\boldsymbol{h}}\cdot\boldsymbol{p}_T\right)-\boldsymbol{k}_T\cdot\boldsymbol{p}_T}{MM_h}h_1^\perp \otimes H_1^\perp\right] \tag{A4}$$

$$F_{UL}^{\sin 2\phi_h} = \left[-\frac{2\left(\hat{\boldsymbol{h}}\cdot\boldsymbol{k}_T\right)\left(\hat{\boldsymbol{h}}\cdot\boldsymbol{p}_T\right)-\boldsymbol{k}_T\cdot\boldsymbol{p}_T}{MM_h}h_{1L}^\perp \otimes H_1^\perp\right] \tag{A5}$$

$$F_{LL} = \left[g_{1L} \otimes D_1\right] \tag{A6}$$

$$F_{UT,T}^{\sin(\phi_h-\phi_S)} = \left[-\frac{\hat{\boldsymbol{h}}\cdot\boldsymbol{p}_T}{M}f_{1T}^\perp \otimes D_1\right] \tag{A7}$$

$$F_{UT,L}^{\sin(\phi_h-\phi_S)} = 0 \tag{A8}$$

$$F_{UT}^{\sin(\phi_h+\phi_S)} = \left[-\frac{\hat{\boldsymbol{h}}\cdot\boldsymbol{k}_T}{M_h}h_1 \otimes H_1^\perp\right] \tag{A9}$$

$$F_{UT}^{\sin(3\phi_h-\phi_S)} = \left[\frac{2\left(\hat{\boldsymbol{h}}\cdot\boldsymbol{p}_T\right)\left(\boldsymbol{p}_T\cdot\boldsymbol{k}_T\right)+\boldsymbol{p}_T^2\left(\hat{\boldsymbol{h}}\cdot\boldsymbol{k}_T\right)-4\left(\hat{\boldsymbol{h}}\cdot\boldsymbol{p}_T\right)^2\left(\hat{\boldsymbol{h}}\cdot\boldsymbol{k}_T\right)}{2M^2M_h}h_{1T}^\perp \otimes H_1^\perp\right] \tag{A10}$$

$$F_{LT}^{\cos(\phi_h-\phi_S)} = \left[\frac{\hat{\boldsymbol{h}}\cdot\boldsymbol{p}_T}{M}g_{1T} \otimes D_1\right] \tag{A11}$$

where the convolution notation $\left[wf \otimes D\right]$ is defined as

$$\left[wf \otimes D\right] \equiv x\sum_a e_a^2 \int d^2\boldsymbol{p}_T\, d^2\boldsymbol{K}_T\, \delta^{(2)}\left(z\boldsymbol{p}_T+\boldsymbol{K}_T-\boldsymbol{P}_{h\perp}\right) w(\boldsymbol{p}_T,\boldsymbol{K}_T)\, f^a(x,p_T^2)\, D^a(z,K_T^2) \tag{A12}$$

For the convenience of the discussions, $\boldsymbol{p}_T$ moments of a general TMD PDF, $f^q(x,p_T^2)$, and FF, $D^q(z,K_T^2)$, are defined [111] as following

$$f^q(x) \equiv \int d^2\boldsymbol{p}_T f^q(x,p_T^2) \tag{A13}$$

$$f^{q(n)}(x) \equiv \int d^2\boldsymbol{p}_T \left(\frac{p_T^2}{2M^2}\right)^n f^q(x,p_T^2) \tag{A14}$$

$$D(z) \equiv \int d^2\boldsymbol{K}_T D^q(z,K_T^2) \tag{A15}$$

$$D^{(n)}(z) \equiv \int d^2\boldsymbol{K}_T \left(\frac{K_T^2}{2z^2M_h^2}\right)^n D^q(z,K_T^2) \tag{A16}$$

Appendix B: PROJECTIONS FOR ALL z-Q^2 BINS

Projections of forty-eight z and Q^2 bins are plotted in Figure 15 to 20.

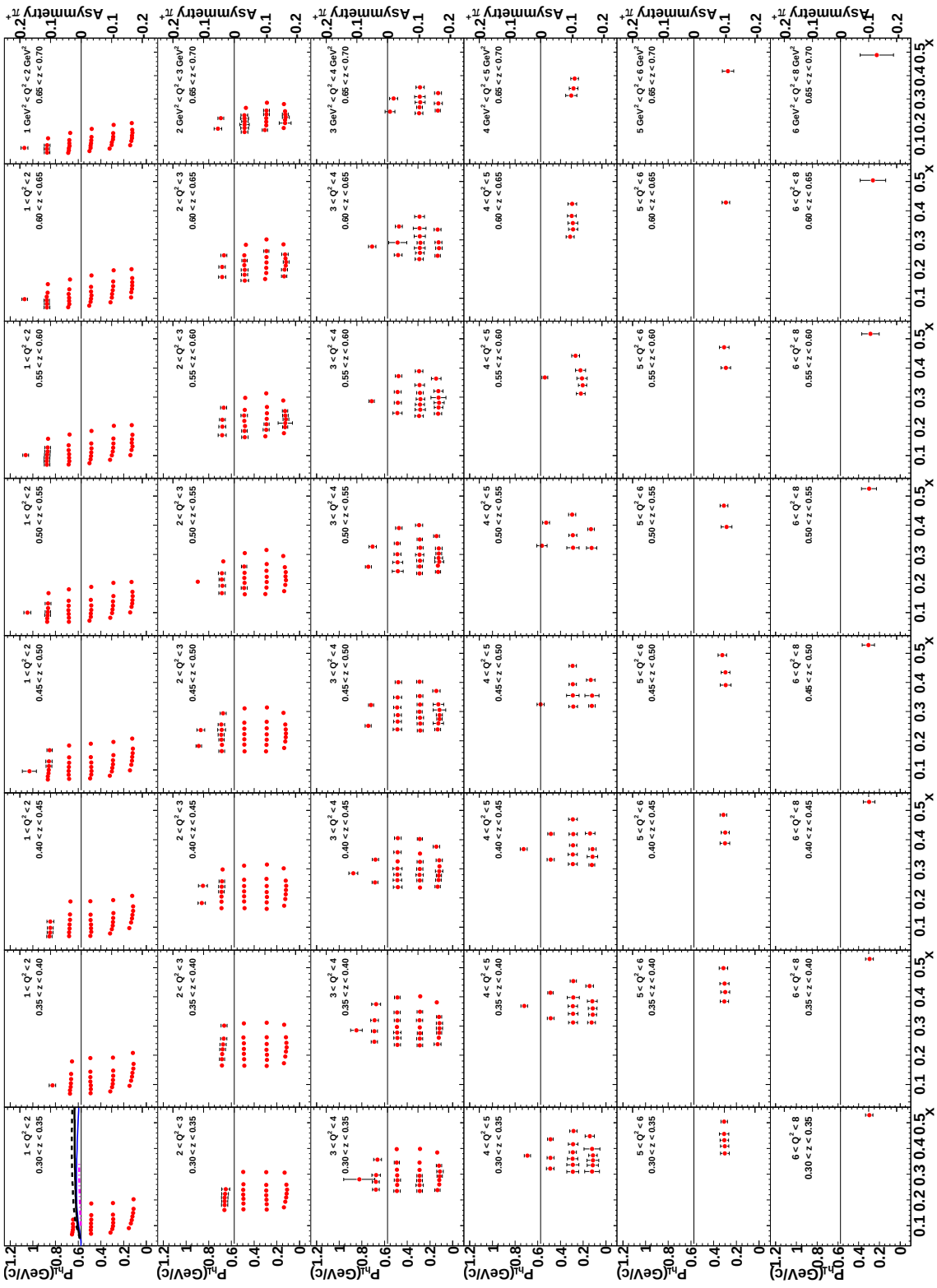

Figure 15: Projections of $A_{UL}^{\sin 2\phi_h}$ for coincidence $e'\pi^+$ channel for all z and Q^2 bins. The legend for these plots is identical to that of Figure 12.

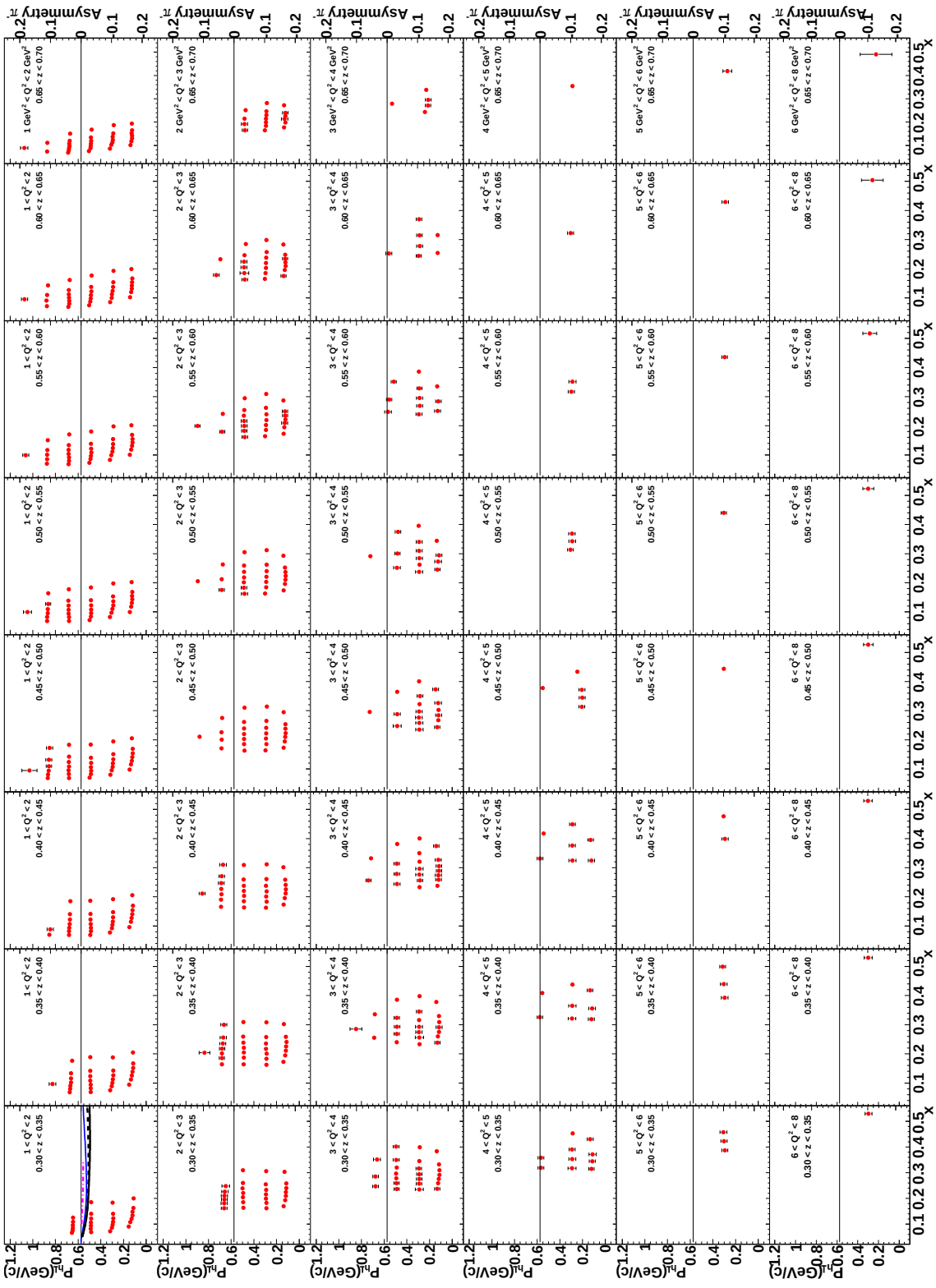

Figure 16: Projections of $A_{UL}^{\sin 2\phi_h}$ for coincidence $e'\pi^-$ channel for all z and Q^2 bins. The legend for these plots is identical to that of Figure 12.

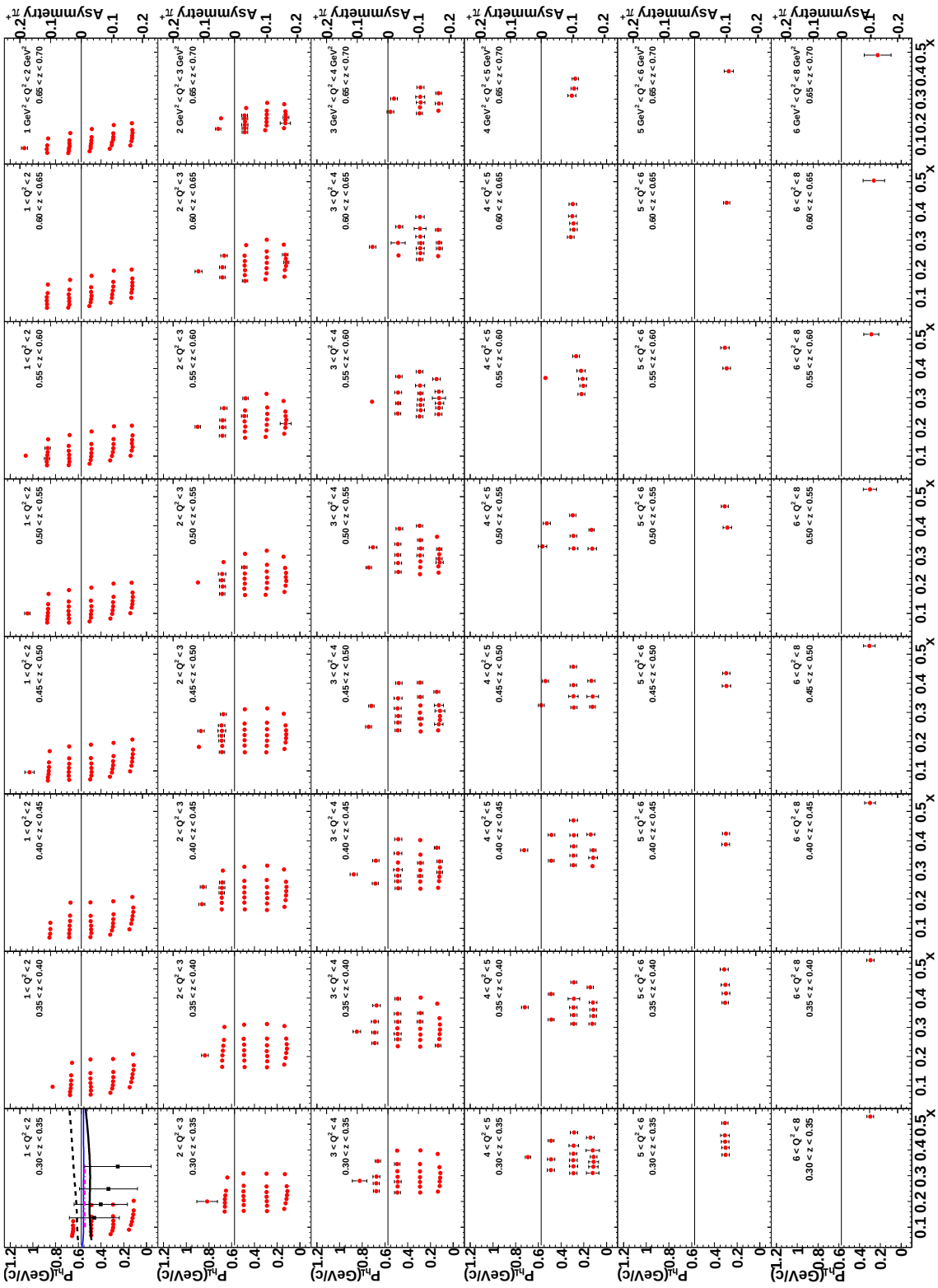

Figure 17: Projections of $A_{LT}^{\cos(\phi_h-\phi_S)}$ for coincidence $e'\pi^+$ channel for all z and Q^2 bins. The legend for these plots is identical to that of Figure 13.

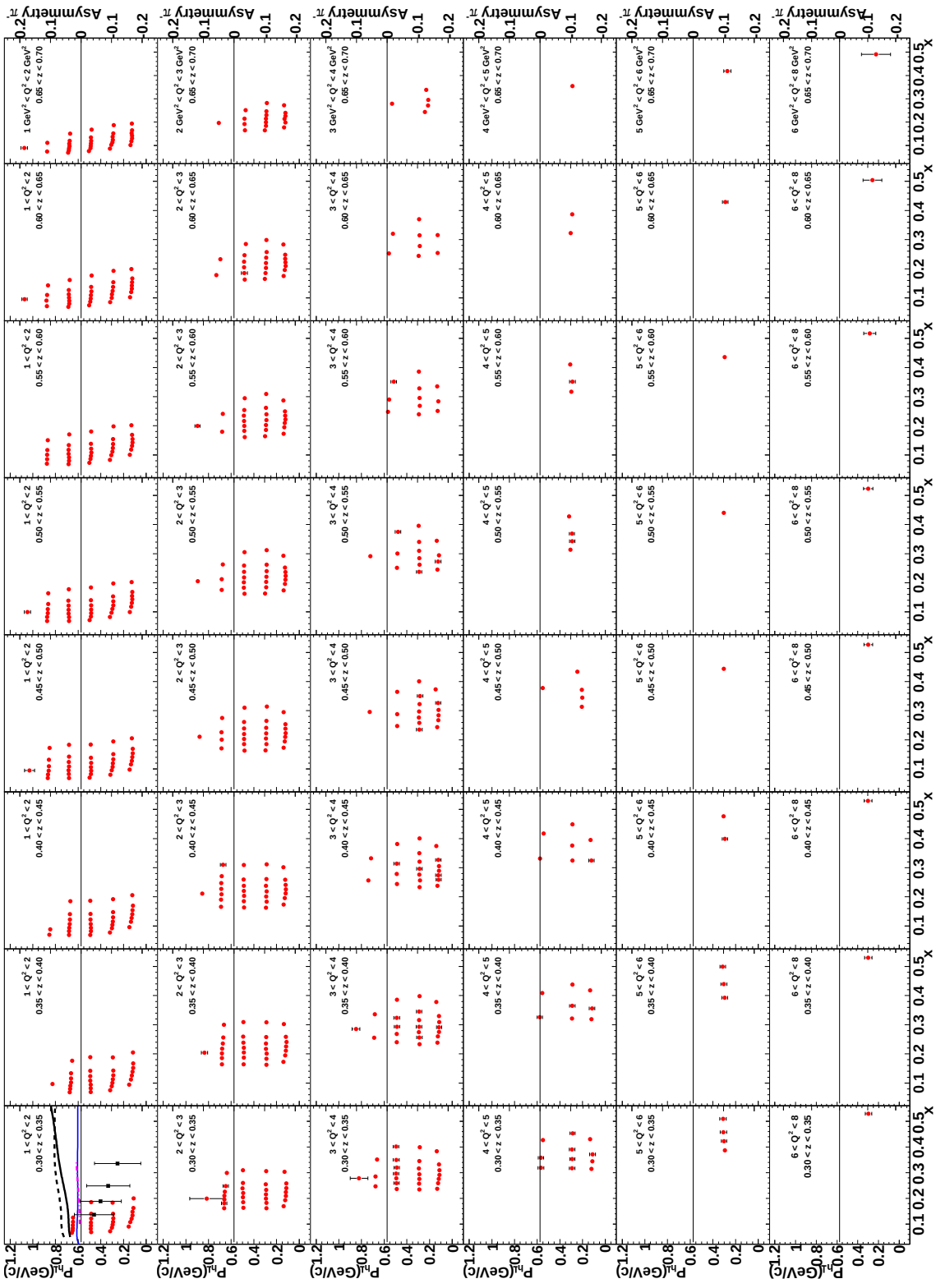

Figure 18: Projections of $A_{LT}^{\cos(\phi_h-\phi_S)}$ for coincidence $e'\pi^-$ channel for all z and Q^2 bins. The legend for these plots is identical to that of Figure 13.

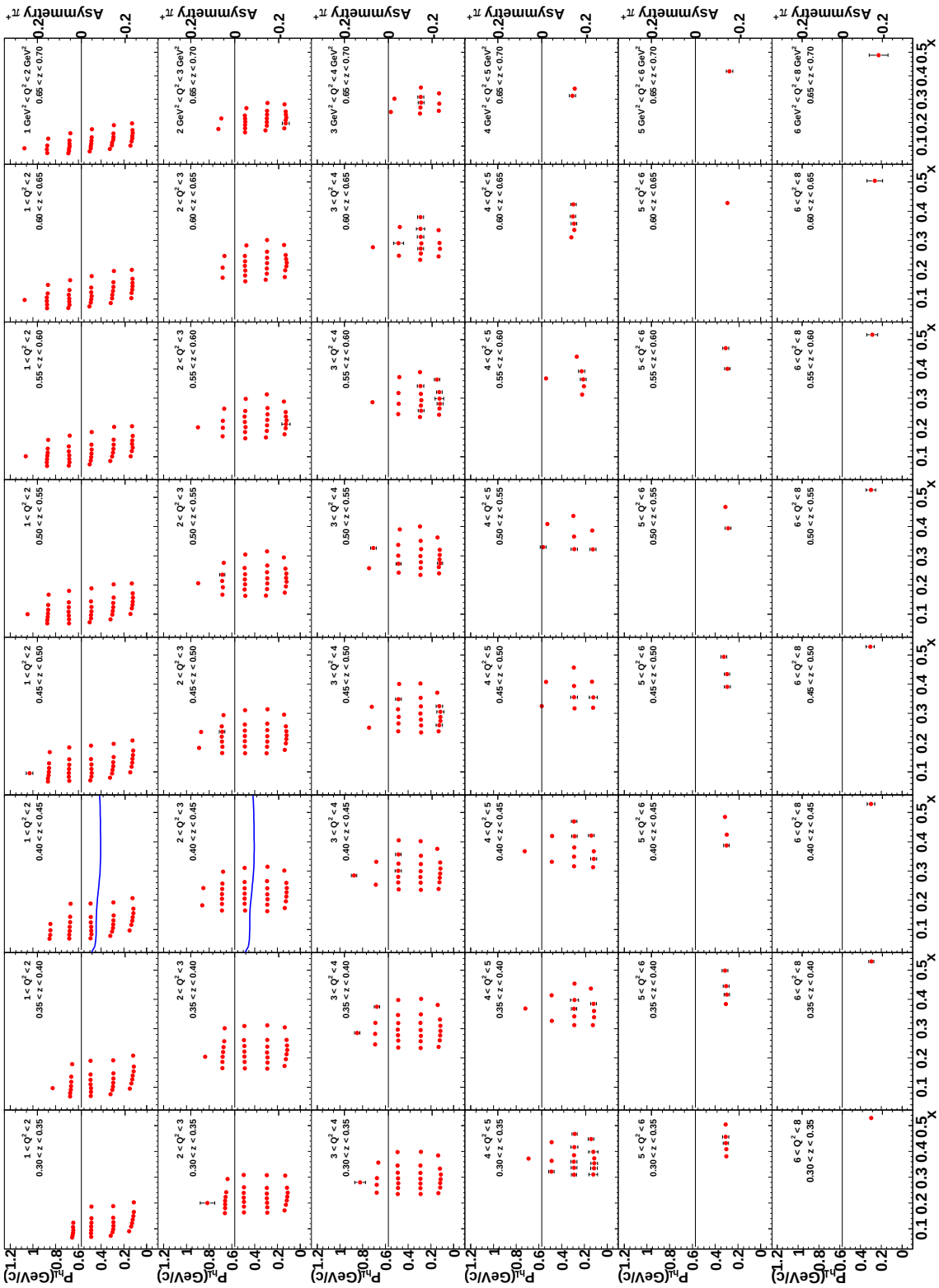

Figure 19: Projections of A_{LL} for coincidence $e'\pi^+$ channel for all z and Q^2 bins. The legend for these plots is identical to that of Figure 14.

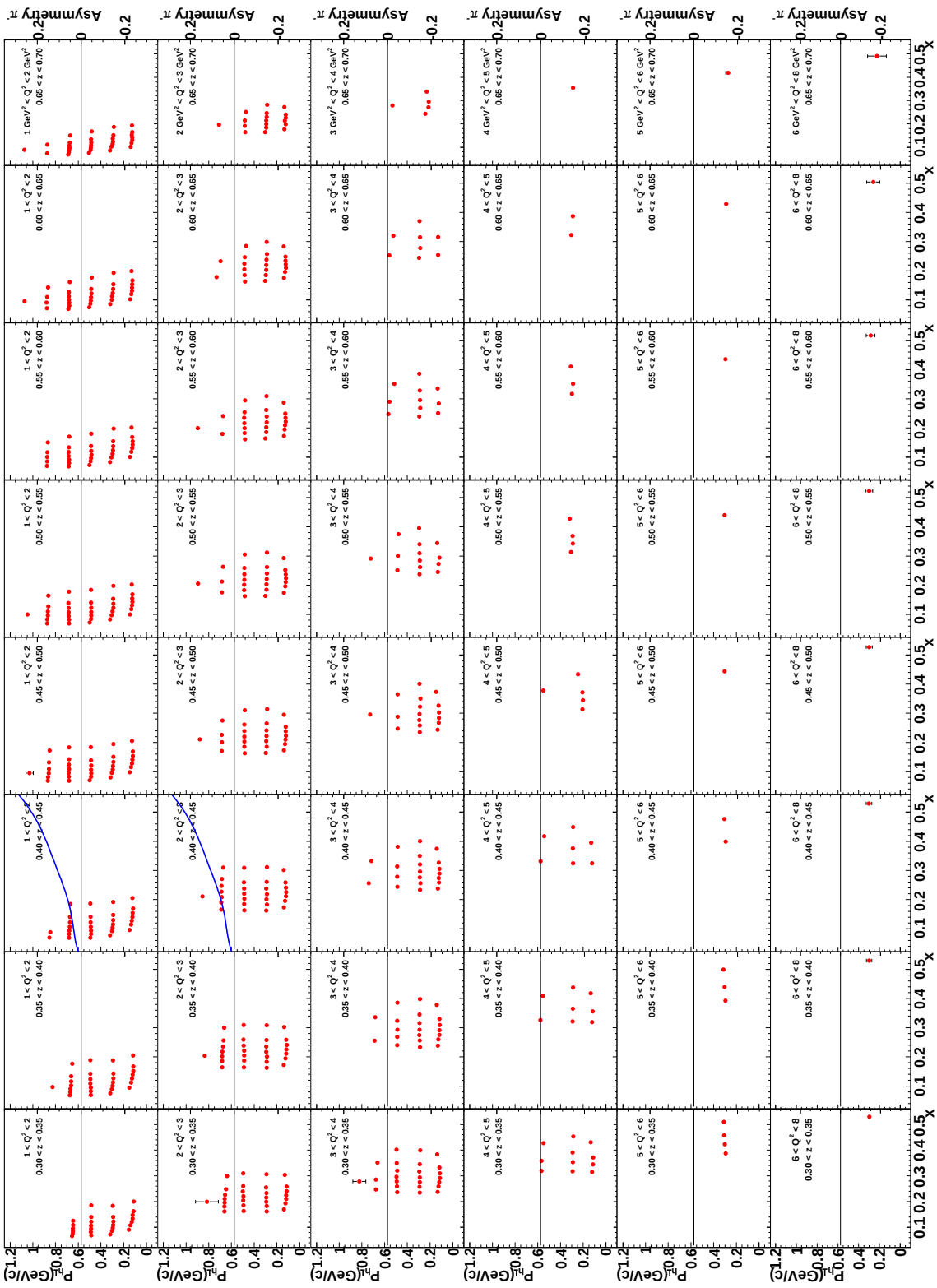

Figure 20: Projections of A_{LL} for coincidence $e'\pi^-$ channel for all z and Q^2 bins. The legend for these plots is identical to that of Figure 14.

Appendix C: ADDITIONAL PLOTS

- Kinematic coverage for 11 GeV (Figure 21) and 8.8 GeV data (Figure 22)
- diffractive ρ production: Figure 23

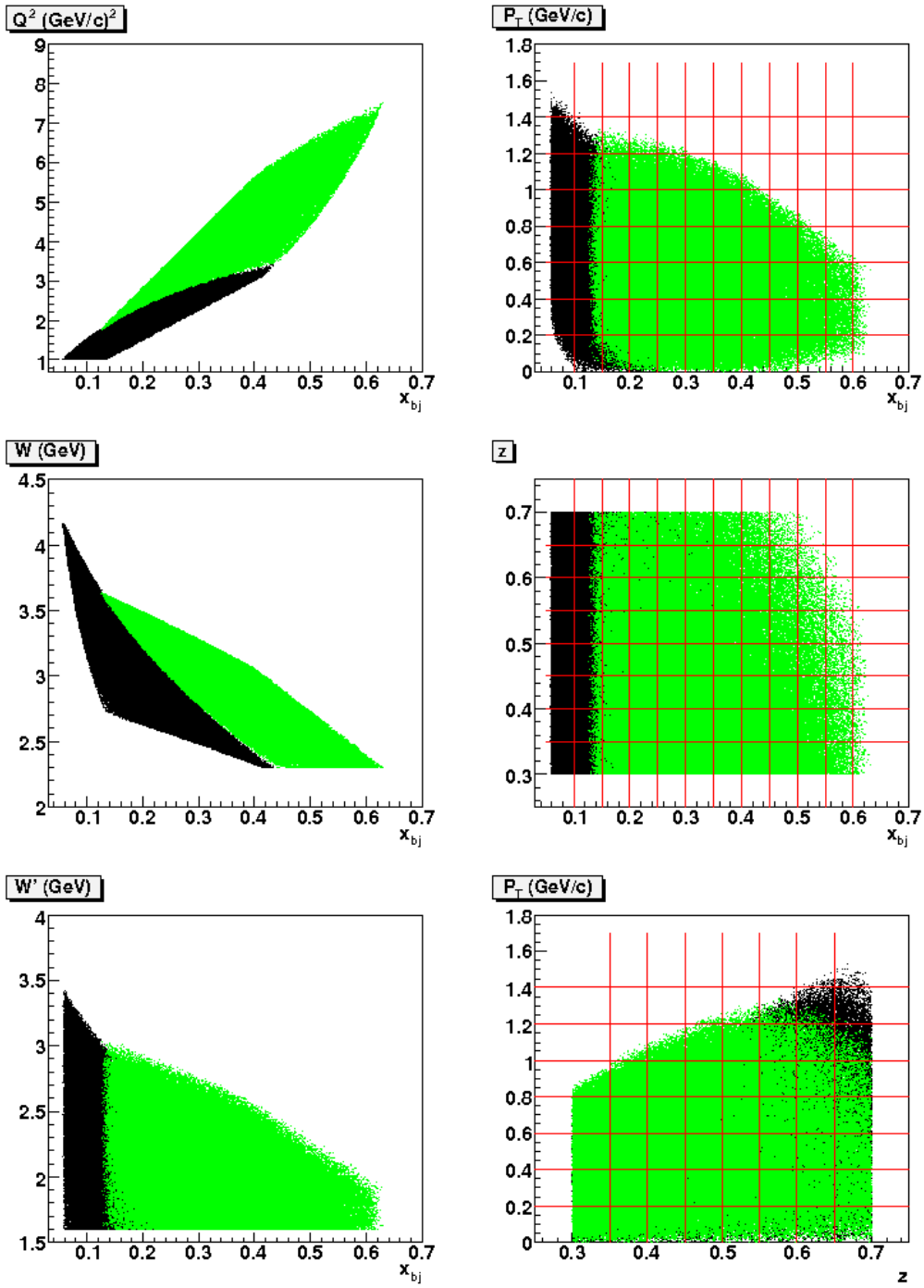

Figure 21: Kinematic coverage for the solenoid detector with a 11 GeV electron beam. The black points show the coverage for the forward-angle detectors and the green points show the coverage for the large-angle detectors. The red grid is the suggested boundaries for kinematic binning. Quoted from [22].

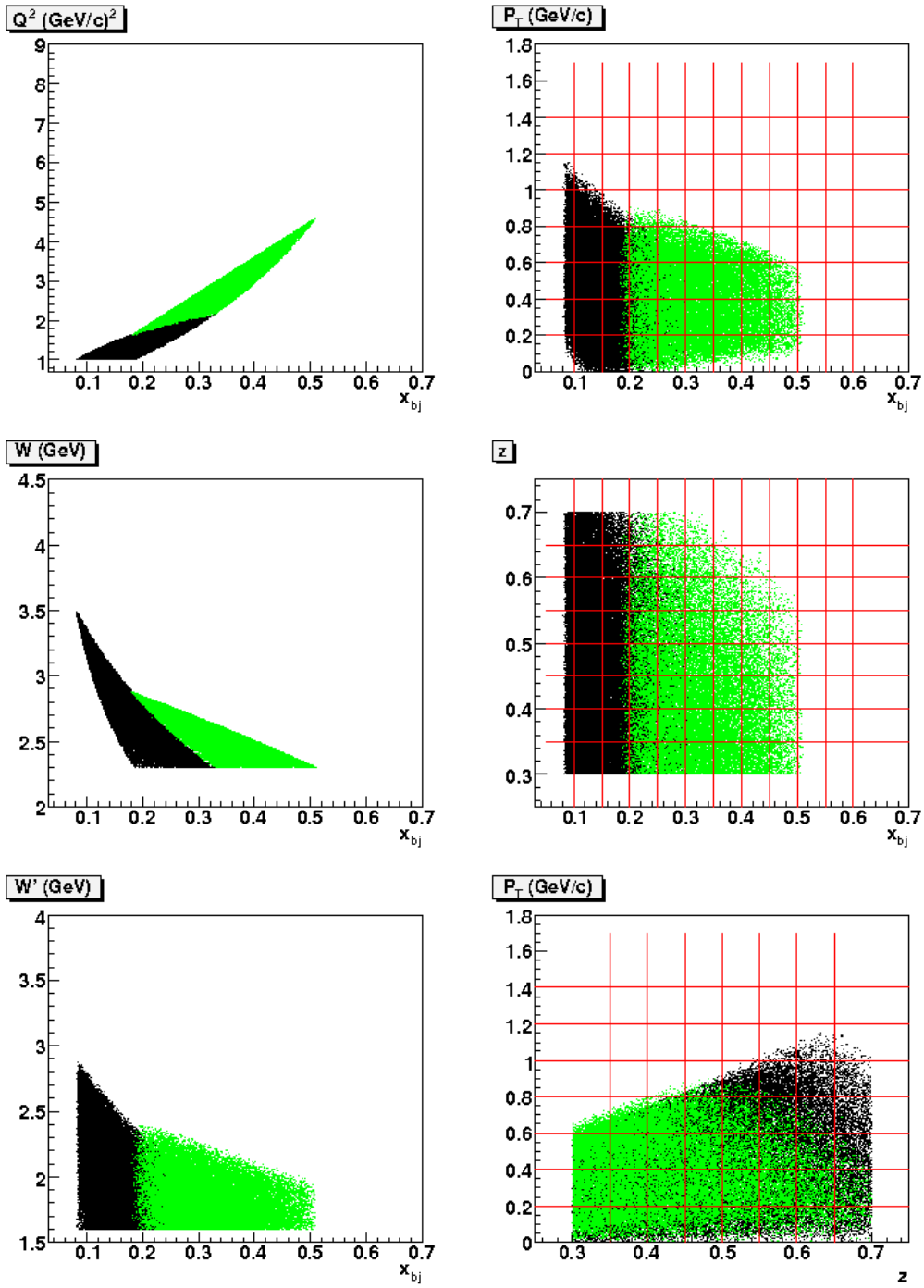

Figure 22: Kinematic coverage for the solenoid detector with a 8.8 GeV electron beam. The black points show the coverage for the forward-angle detectors and the green points show the coverage for the large-angle detectors. The red grid is the suggested boundaries for kinematic binning. Quoted from [22].

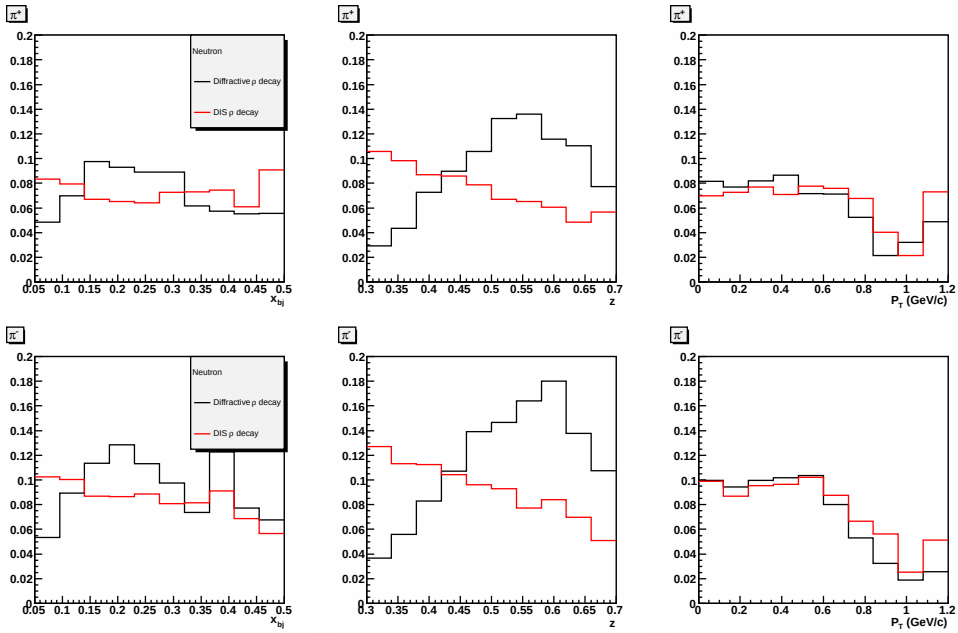

Figure 23: The black curve shows the contamination from the diffractive ρ production for neutron $\pi^{\pm}$ contamination, quoted from a study in [22].

---

[1] K. Nakamura and P. D. Group, Journal of Physics G: Nuclear and Particle Physics **37**, 075021 (2010).

[2] J. Ashman et al. (European Muon), Phys. Lett. **B206**, 364 (1988).

[3] X. Ji, J.-P. Ma, and F. Yuan, Nuclear Physics B **652**, 383 (2003).

[4] A. Bacchetta, F. Conti, and M. Radici, Phys. Rev. **D78**, 074010 (2008), 0807.0323.

[5] B. Pasquini, S. Cazzaniga, and S. Boffi, Phys. Rev. D **78**, 034025 (2008).

[6] S. Boffi, A. V. Efremov, B. Pasquini, and P. Schweitzer, Phys. Rev. D **79**, 094012 (2009).

[7] A. Bravar, Nuclear Physics B - Proceedings Supplements **79**, 520 (1999), proceedings of the 7th International Workshop on Deep Inelastic Scattering and QCD.

[8] null HERMES Collaboration and A. Airapetian, Phys.Rev.D **64:097101,2001** (2001), hep-ex/0104005.

[9] A. Airapetian, N. Akopov, M. Amarian, E. C. Aschenauer, H. Avakian, R. Avakian, A. Avetissian, E. Avetissian, B. Bains, C. Baumgarten, et al. ((The HERMES Collaboration)), Phys. Rev. Lett. **84**, 4047 (2000).

[10] H. Avakian et al. (CLAS), Phys. Rev. **D69**, 112004 (2004), hep-ex/0301005.

[11] H. Avakian and L. Elouadrhiri (CLAS), Phys. Part. Nucl. **35**, S114 (2004).

[12] A. Airapetian et al. (HERMES), Phys. Rev. Lett. **94**, 012002 (2005), hep-ex/0408013.

[13] M. G. Alekseev et al. (The COMPASS), Phys. Lett. **B692**, 240 (2010), 1005.5609.

[14] V. Y. Alexakhin et al. (COMPASS), Phys. Rev. Lett. **94**, 202002 (2005), hep-ex/0503002.

[15] A. Kotzinian (on behalf of the COMPASS) (2007), 0705.2402.

[16] J. Huang, in *12th International Conference on Meson-Nucleon Physics and the Structure of the Nucleon* (2010), URL http://conferences.jlab.org/menu10/talks/Monday%20-%20Parallel%20Sessions/Session%202C%20Spin%20Structure%202/Jin%20Huang%20MENU.pdf.

[17] X. Jiang, in *12th International Conference on Meson-Nucleon Physics and the Structure of the Nucleon* (2010), URL http://conferences.jlab.org/menu10/talks/Thursday%20-%20Plenary/xjiang_menu2010.pdf.

[18] A. Airapetian et al. (HERMES), Phys. Lett. **B562**, 182 (2003), hep-ex/0212039.

[19] A. Airapetian et al. (HERMES), Phys. Lett. **B622**, 14 (2005), hep-ex/0505042.

[20] M. Alekseev, V. Alexakhin, and Y. Alexandrov, The European Physical Journal C - Particles and Fields pp. 1–11 (2010), 10.1140/epjc/s10052-010-1461-9.

[21] H. Avakian et al. (The CLAS) (2010), 1003.4549.

[22] J. P. Chen, H. Gao, X. Jiang, J. Peng, X. Qian, and et al, *JLab E12-10-006 : Target Single Spin Asymmetry in Semi-Inclusive Deep-Inelastic Electro Pion Production on a Trasversely Polarized 3He Target at 8.8 and 11 GeV, An update to PR12-09-014* (2010), URL http://www.jlab.org/exp_prog/proposals/10/PR12-10-006.pdf.

[23] H. Avagyan, K. Joo, Z. E. Meziani, B. Seitz, and et al, *JLab E12-06-112 : Probing the Proton's Quark Dynamics in Semi-Inclusive Pion Production at 12 GeV* (2006), URL http://www.jlab.org/exp_prog/proposals/09/PR12-06-112.pdf.

[24] H. Avakian, P. Bosted, K. Griffioen, K. Hafidi, P. Rossi, and et al, *JLab E12-07-107 : Studies of Spin-Orbit Correlations with Longitudinally Polarized Target* (2007), URL http://www.jlab.org/exp_prog/proposals/07/PR12-07-107.pdf.

[25] H. Avagyan, F. Benmokhtar, M. E. Alaoui, K. Hafidi, and M. M. et al, *JLAB E12-09-007 : Studies of partonic distributions using semi-inclusive production of kaons* (2009), URL http://www.jlab.org/exp_prog/proposals/09/PR12-09-007.pdf.

[26] H. Avagyan, M. Contalbrigo, K. Joo, Z. E. Meziani, B. Seitz, and et al, *JLab E12-09-008 : Studies of the Boer-Mulders Asymmetry in Kaon Electroproduction with Hydrogen and Deuterium Targets* (2009), URL http://www.jlab.org/exp_prog/proposals/09/PR12-09-008.pdf.

[27] H. Avagyan, M. Contalbrigo, K. Joo, Z. E. Meziani, B. Seitz, and et al, *JLab E12-09-009 : Studies of Spin-Orbit Correlations in Kaon Electroproduction in DIS with polarized hydrogen and deuterium targets* (2009), URL http://www.jlab.org/exp_prog/proposals/09/PR12-09-009.pdf.

[28] A. Bacchetta, U. D'Alesio, M. Diehl, and C. A. Miller, Phys. Rev. D **70**, 117504 (2004).

[29] A. Bacchetta, M. Diehl, K. Goeke, A. Metz, P. J. Mulders, and M. Schlegel, Journal of High Energy Physics **2007**, 093 (2007), hep-ph/0611265.

[30] M. Diehl and S. Sapeta, Eur. Phys. J. **C41**, 515 (2005), hep-ph/0503023.

[31] P. J. Mulders and R. D. Tangerman, Nuclear Physics B **461**, 197 (1996).

[32] D. Boer and P. J. Mulders, Phys. Rev. **D57**, 5780 (1998), hep-ph/9711485.

[33] A. Bacchetta, in *Spin 2008* (2008), URL https://collab.itc.virginia.edu/access/content/group/c876276f-5a6e-4cc5-80aa-96edb60105ec/Parallel%20Talks/Nucleon%20Structure%20-%20Transverse%20Spin/bacchetta_spin08-1.pdf.

[34] M. Diehl and P. Hägler, The European Physical Journal C - Particles and Fields **44**, 87 (2005), 10.1140/epjc/s2005-02342-6.

[35] B. Pasquini and C. Lorce, in *The 4th Workshop on Exclusive Reactions at High Momentum Transfer* (Jefferson Lab, 2010), 1008.0945, URL http://conferences.jlab.org/exclusive2010/talks/Friday/Pasquini_Jlab.pptx.

[36] B. Pasquini and C. Lorce, in *GPD workshop at Trento* (2010), URL http://wwwcompass.cern.ch/compass/gpd/Conf_Trento_2010/5thday/Pasquini_GPD10_2003.ppt.

[37] J. W. N. Ph. Hägler, B. U. Musch and A. Schäfer, EPL (Europhysics Letters) **88**, 61001 (2009).

[38] A. Bacchetta, M. Boglione, A. Henneman, and P. J. Mulders, Phys. Rev. Lett. **85**, 712 (2000).

[39] A. Bacchetta, M. Radici, F. Conti, and M. Guagnelli, Eur. Phys. J. **A45**, 373 (2010), 1003.1328.

[40] B. U. Musch, P. Hagler, J. W. Negele, and A. Schafer (2010), 1011.1213.

[41] R. Jakob, P. J. Mulders, and J. Rodrigues, Nuclear Physics A **626**, 937 (1997).

[42] A. Kotzinian, B. Parsamyan, and A. Prokudin, Phys. Rev. D **73**, 114017 (2006).

[43] A. V. Efremov, P. Schweitzer, O. V. Teryaev, and P. Zavada, Phys. Rev. **D80**, 014021 (2009), 0903.3490.

[44] H. Avakian, A. V. Efremov, P. Schweitzer, and F. Yuan, Phys. Rev. D **81**, 074035 (2010).

[45] S. Meissner, A. Metz, and K. Goeke, Phys. Rev. **D76**, 034002 (2007), hep-ph/0703176.

[46] K. Goeke, A. Metz, P. V. Pobylitsa, and M. V. Polyakov, Physics Letters B **567**, 27 (2003).

[47] A. Metz, P. Schweitzer, and T. Teckentrup, Physics Letters B **680**, 141 (2009).

[48] U. D'Alesio, E. Leader, and F. Murgia, Phys. Rev. **D81**, 036010 (2010), 0909.5650.

[49] S. Wandzura and F. Wilczek, Phys. Lett. **B72**, 195 (1977).

[50] H. Avakian, A. V. Efremov, K. Goeke, A. Metz, P. Schweitzer, and T. Teckentrup, Phys. Rev. D **77**, 014023 (2008).

[51] A. M. Kotzinian and P. J. Mulders, Phys. Rev. D **54**, 1229 (1996).

[52] H. Avakian, A. Kotzinian, B. U. Musch, A. Prokudin, and P. Schweitzer (2010), in Preparation.

[53] A. Efremov, K. Goeke, and P. Schweitzer, Czechoslovak Journal of Physics **55**, A189 (2005), 10.1007/BF03032004.

[54] A. Efremov, K. Goeke, and P. Schweitzer, The European Physical Journal C - Particles and Fields **24**, 407 (2002), 10.1007/s100520200918.

[55] A. Accardi, A. Bacchetta, W. Melnitchouk, and M. Schlegel, JHEP **11**, 093 (2009), 0907.2942.

[56] L. P. Gamberg, G. R. Goldstein, and M. Schlegel, Phys. Rev. **D77**, 094016 (2008), 0708.0324.

[57] A. Bacchetta, D. Boer, M. Diehl, and P. J. Mulders, JHEP **08**, 023 (2008), 0803.0227.

[58] B. Parsamyan, The European Physical Journal - Special Topics **162**, 89 (2008), 10.1140/epjst/e2008-00780-1.

[59] H. Avakian et al. (The CLAS) (2010), 1003.4549.

[60] A. V. Efremov, K. Goeke, and P. Schweitzer, Phys. Rev. D **73**, 094025 (2006).

[61] J. She, J. Zhu, and B.-Q. Ma, Phys. Rev. **D79**, 054008 (2009), 0902.3718.

[62] J. Zhu and B.-Q. Ma (2010), in Preparation.

[63] D. de Florian, R. Sassot, M. Stratmann, and W. Vogelsang, Phys. Rev. **D80**, 034030 (2009), 0904.3821.

[64] D. de Florian, R. Sassot, M. Stratmann, and W. Vogelsang, Phys. Rev. Lett. **101**, 072001

(2008).

[65] M. Hirai and S. Kumano (Asymmetry Analysis), Nucl. Phys. **B813**, 106 (2009), 0808.0413.

[66] E. Leader, A. V. Sidorov, and D. B. Stamenov, Phys. Rev. **D75**, 074027 (2007), hep-ph/0612360.

[67] J. M. Niczyporuk and E. E. W. Bruins, Phys. Rev. **D58**, 091501 (1998), hep-ph/9804323.

[68] E. Christova and E. Leader, Phys. Lett. **B468**, 299 (1999), hep-ph/9907265.

[69] E. Christova and E. Leader, Nucl. Phys. **B607**, 369 (2001), hep-ph/0007303.

[70] J. P. Chen and X. Jiang, *The delta d experiment: Constraining d-quark polarization through semi-inclusive spin asymmetry measurements on a polarized helium-3 target*, JLAB 12GeV Proposal (2009), URL http://www.jlab.org/exp_prog/proposals/09/PR12-09-013.pdf.

[71] X. Zheng et al. (Jefferson Lab Hall A), Phys. Rev. Lett. **92**, 012004 (2004), nucl-ex/0308011.

[72] X. Zheng et al. (Jefferson Lab Hall A), Phys. Rev. **C70**, 065207 (2004), nucl-ex/0405006.

[73] M. Anselmino, A. Efremov, A. Kotzinian, and B. Parsamyan, Phys. Rev. **D74**, 074015 (2006), hep-ph/0608048.

[74] H. Avakian, S. J. Brodsky, A. Deur, and F. Yuan, Phys. Rev. Lett. **99**, 082001 (2007), 0705.1553.

[75] B.-Q. Ma, I. Schmidt, and J.-J. Yang, Phys. Rev. **D66**, 094001 (2002), hep-ph/0209114.

[76] G. S. Atoian et al., Nucl. Instrum. Meth. **A531**, 467 (2004), physics/0310047.

[77] G. S. Atoian et al., Nucl. Instrum. Meth. **A584**, 291 (2008), 0709.4514.

[78] H. Gao et al., *JLab E06-010: Measurement of Single Target-Spin Asymmetry in Semi-Inclusive Pion Electroproduction on a Transversely Polarized* ^{3}*He Target* (2006), JLab E06-010, URL http://www.jlab.org/exp_prog/proposals/06/PR06-010.pdf.

[79] S. Choi, X. Jiang, Z. E. Meziani, B. Sawatzky, et al., *JLab E06-014: Precision Measurements of the Neutron dc: Towards the Electric XE and Magnetic XB Color Polarizabilities* (2006), URL http://www.jlab.org/exp_prog/proposals/06/PR06-014.pdf.

[80] T. Averett, J. P. Chen, X. Jiang, et al., *JLab E05-015: Measurement of the Target Single-Spin Asymmetry in Quasi-Elastic* ^{3}*He(e,e)́* (2005), URL http://www.jlab.org/exp_prog/proposals/05/PR05-015.pdf.

[81] S. Gilad, D. Higinbotham, W. Korsch, B. Norum, S. Sirca, et al., *JLab E05-102: Measurements of Ax and Az Asymmetries in the Quasi-elastic* ^{3}*He(e,ed́) Reaction* (2005), URL http://www.jlab.org/exp_prog/proposals/05/PR05-102.pdf.

[82] M. C. Altunbas et al., Nucl. Instrum. Meth. **A490**, 177 (2002).

[83] P. Abbon et al. (COMPASS), Nucl. Instrum. Meth. **A577**, 455 (2007), hep-ex/0703049.

[84] Y. Wang et al., Chin. Phys. **C33**, 374 (2009).

[85] P. Souder et al., *JLab E12-10-007 : Precision Measurement of Parity-Violation in Deep Inelastic Scattering Over a Broad Kinematic Range* (2010), URL http://www.jlab.org/exp_prog/proposals/10/PR12-10-007.pdf.

[86] X. Qian et al. (JLab E12-10-006), Tech. Rep., Jefferson Lab (2009), ϕ_h Coverage Plots for SoLID TMD Measurements (username: **12transversity**; password: **SoLID**)., URL http://www.jlab.org/~xqian/SoLID/phi_coverage.pdf.

[87] J. Huang and Y. Qiang, *Maximum likelihood estimation of asymmetry and angular modulation for transversity* (2010), URL http://www.jlab.org/~jinhuang/Transversity/MLE.pdf.

[88] X. Qian, Ph.D. thesis, Duke University (2010).

[89] J. L. Friar, B. F. Gibson, G. L. Payne, A. M. Bernstein, and T. E. Chupp, Phys. Rev. **C42**, 2310 (1990).

[90] C. Ciofi degli Atti, S. Scopetta, E. Pace, and G. Salme, Phys. Rev. **C48**, 968 (1993), nucl-th/9303016.

[91] F. R. P. Bissey, A. W. Thomas, and I. R. Afnan, Phys. Rev. **C64**, 024004 (2001), nucl-th/0012081.

[92] A. Nogga, Ph.D. thesis, Ruhr-Universität Bochum, Bochum, Germany (2001), p. 72.

[93] B.-Q. Ma, J. Phys. **G17**, L53 (1991), 0711.2335.

[94] B.-Q. Ma, Z. Phys. **C58**, 479 (1993), hep-ph/9306241.

[95] A. D. Martin, W. J. Stirling, R. S. Thorne, and G. Watt, Eur. Phys. J. **C63**, 189 (2009), 0901.0002.

[96] J. Blumlein and H. Bottcher, Nucl. Phys. **B636**, 225 (2002), hep-ph/0203155.

[97] D. de Florian, R. Sassot, and M. Stratmann, Phys. Rev. **D75**, 114010 (2007), hep-ph/0703242.

[98] X.-d. Ji, J.-P. Ma, and F. Yuan, Phys. Lett. **B597**, 299 (2004), hep-ph/0405085.

[99] X.-d. Ji, J.-p. Ma, and F. Yuan, Phys. Rev. **D71**, 034005 (2005), hep-ph/0404183.

[100] L. A. Linden-levy, Ph.D. thesis, UIUC (2008).

[101] H. Avakian, V. Burkert, L. Elouadrhiri, N. Bianchi, G. Adams, A. Afanasev, P. Ambrozewicz,

E. Anciant, M. Anghinolfi, D. Armstrong, et al. ((CLAS Collaboration)), Phys. Rev. D **69**, 112004 (2004).

[102] J. P. Chen, H. Gao, X. Jiang, J. Peng, X. Qian, and et al, *JLab PR12-09-014 : Target Single Spin Asymmetry in Semi-Inclusive Deep-Inelastic Electro Pion Production on a Trasversely Polarized 3He Target at 11 GeV* (2010), URL http://www.jlab.org/exp_prog/proposals/09/PR12-09-014.pdf.

[103] B. Andersson, G. Gustafson, G. Ingelman, and T. Sjostrand, Phys. Rept. **97**, 31 (1983).

[104] I. Akushevich, A. Ilyichev, and N. Shumeiko (2001), hep-ph/0106180.

[105] During an asymmetry measurement, the $F_{UU}^{\cos\phi_h}$ and $F_{UU}^{\cos 2\phi_h}$ functions do not flip their signs with the spin/helicity flips. Therefore, they only contribute as a dilution effect, from an effective modification to the unpolarized cross section. Further, if the ϕ_h coverage is large, the dilution effect is further suppressed since2π integral of $F_{UU}^{\cos\phi_h}$ and $F_{UU}^{\cos 2\phi_h}$ is zero. This effect can be directly studied and corrected by including $F_{UU}^{\cos\phi_h}$ and $F_{UU}^{\cos 2\phi_h}$ into the fitting procedure.

[106] Equations (21) and (22) also hold in the Covariant Parton Model [43], upon the neglect of current quark mass terms.

[107] This analysis use NLO global parametrization of unpolarized PDF [95], polarized PDF [96] and unpolarized FF [97]. The asymmetries were calculated at $Q^2 = 2.0$ GeV^2 and $z = 0.425$.

[108] based on experience of on-going target analysis of 6GeV Transversity experiment [78]

[109] The full width resolution of calibrated coincidence timing peak for forward angle particle coincidence is expected to be better than 0.5 ns due to use of MRPC. However, for electrons detected at large angles, the timing was provided by calorimeter, whose timing resolution is on the ns level. Therefore, we quote a 6 ns coincidence timing window over the whole acceptance for the systematic uncertainty estimations.

[110] The average vertex resolution is $\sigma \lesssim 1.5$ cm as shown on Figure 14 of [22]. Therefore, the background suppress due to vertex coincidence is 40 cm (target length)$/6\sigma \gtrsim 4$.

[111] Using, e.g., a Gaussian parametrization of the transverse momentum dependence as a working assumption, the integrals for the TMD moments are well-defined.